Detection of Faulty Elements in IC-Controlled Phased Arrays Using Sparse Far-Field Data: A Machine-Learning Approach

Aparna Kannan

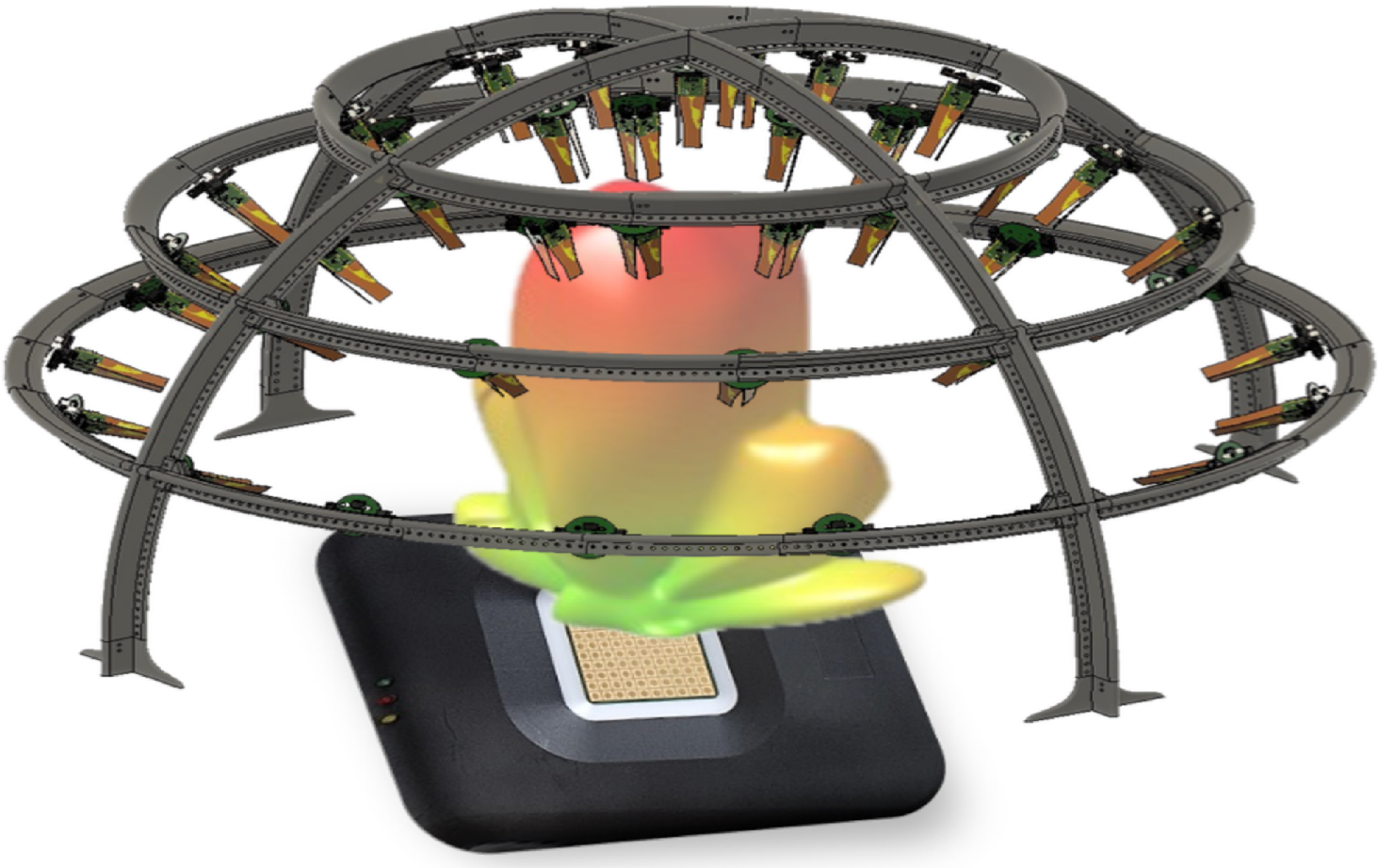

Delft University of Technology

Detection of Faulty Elements in IC-Controlled Phased Arrays Using Sparse Far-Field Data: A Machine-Learning Approach

by

Aparna Kannan

to obtain the degree of Master of Science
at the Delft University of Technology,
to be defended publicly on September 11, 2024 at 13:30 PM.

Student No.:	5476763
Daily Supervisor:	Dr. Yanki Aslan
Daily Supervisor:	Ir. Berk Onat
External Supervisor:	Dr. Marco Spirito
Thesis committee:	Prof. DSc. Alexander Yarovoy, Professor, Chairman MS3-EWI
	Dr. Geethu Joseph, Assistant Professor SPS-EWI
	Dr. Yanki Aslan, Assistant Professor MS3-EWI
	Dr. Marco Spirito, Associate Professor ELCA-EWI
Faculty:	Electrical Engineering, Mathematics and Computer Science, Delft

An electronic version of this thesis is available at: http://repository.tudelft.nl/
Cover page image: Modified Antenna Dome Real-time Distributed Antenna Pattern Characterization System.

TU Delft

Acknowledgements

This part of the thesis is dedicated to thanking all the people who have provided their unwavering support and guidance throughout this endeavour. This thesis is a testimony to the hard work and efforts taken towards contributing to the scientific community. I have learnt a lot throughout this journey from my supervisors, peers and family, who guided me personally and professionally.

I am extremely thankful to Prof. DSc Alexander Yarovoy for giving me the opportunity to work with the Microwave Sensing, Signals and Systems (MS3) group for my thesis. Thank you for always making me feel comfortable with your constant encouragement and stimulating mentorship. The research environment you have provided for this thesis truly helped and motivated me for the duration of this thesis.

My daily supervisor, Dr. Yanki Aslan, provided invaluable insights and feedback during every meeting and helped enrich the quality of this work. Your invaluable support and keen insight have challenged me to critically analyze my work and have shaped my approach to scientific research in this field.

I am very grateful to ir. Berk Onat for your invaluable guidance and contributions during our meetings; your dedication to bringing this thesis to completion helped me immensely. I would also like to thank the MS3 family for being such a cheerful and supportive environment; appreciate all the insight and knowledge I have gained through the weekly seminars.

I thank Dr. Marco Spirito, my external supervisor, for providing the Measurement setup and guidance throughout this stage. Your input and guidance during our joint discussions regarding the Antenna Dome were highly beneficial. A special thanks to ir. Mate Ivanyi for working with me on the measurement data collection and for your feedback and comments during our discussions.

I am deeply grateful for the unwavering support and kindness shown by my friends and colleagues throughout this Masters course. Your empathy and company during the ups and downs of this journey made all of this possible.

Finally, I would like to thank my family for always believing in me and being my source of motivation during this journey. Your constant love and faith helped me through almost every difficulty and made me the person I am today.

Thank you everyone.

Aparna Kannan
Delft, September 2024

Summary

Active phased array antennas, generally consisting of a large number of antenna elements and integrated-circuit (IC) components, are essential for different applications like 5G/6G communications, radar, aerospace, satellite communications and so on. The study of radiation pattern measurements and analysis of pattern data is a pivotal step in characterizing and understanding the use of antennas in any application.

Unwanted changes can be observed in the radiation pattern due to randomly failed elements, ICs, or IC channels in phased arrays. Hence, there is a vital need for fast testing and diagnosis to identify possible failures of these large antenna systems, before taking any immediate action to compensate for these changes. Due to integrated-circuits (IC) non-linearities and mutual coupling challenges, the existing deterministic and optimization-based fault detection techniques fail to provide reliable results in practical systems. Besides, it is desired to achieve real-time array diagnosis during in-field operation, which makes the problem even more challenging.

In this thesis, a novel machine-learning assisted fault-detection algorithm is proposed which is trained by using sparse far-field measurements from a practical IC-integrated millimeter-wave (mm-wave) phased array prototype and fixed multi-probe measurement system (antenna dome). A global optimization approach is used as a benchmark for comparison to the state-of-the-art. The incorporation of machine learning techniques greatly improves the fault detection time and accuracy in comparison to global optimizers. Based on the measured randomized dataset with 8 faulty elements in a 64-element array, It is demonstrated that the proposed machine learning approach significantly outperforms the existing global optimization techniques by improving the average detection success ratio from about 50% to 80%, while promising real-time detection. Furthermore, studies based on the number of sampling points used and the varying number of faults are also conducted which indicates similar conclusions.

Contents

List of Figures

List of Tables

Nomenclature

Abbreviations

Abbreviation	Definition
EM	Electromagnetic
IC	Integrated Circuit
AUT	Antenna Under Test
SLL	Sidelobe Level
PA	Power Amplifier
CS	Compressed Sensing
SR	Sparse recovery
CST	Computer Simulation Technology
AF	Array Factor
EEP	Embedded Element Pattern
AEP	Array Element Pattern
IEP	Isolated Element Pattern
ELCA	Electronic Research Laboratory
DUCAT	Delft University Chamber for Antenna Tests
SAR	Synthetic Aperture Radar
BTM	Back Transformation method
MM	Matrix Method
GA	Genetic Algorithm
PSO	Particle Swarm Optimization
MLP	Multi-Layer Perceptron
CNN	Convolutional Neural Networks
SVM	Support Vector Machine
ANN	Artificial Neural Network
MSE	Mean Squared Error
SNR	Signal-to-Noise-Ratio
MC	Mutual Coupling
ML	Machine Learning
ReLU	Rectified Error Linear Units
GeLU	Gaussian Error Linear Units
OTA	Over the Air

1

Introduction

Active phased arrays consist of antennas, electronics and feeding circuits which are used to control the antenna's main beam without any physical intervention. Thus, the beam can be directed at a target based on its coordinates without the need for complex tactical equipment or traditional search methods. The study of active phased arrays controlled by integrated-circuits (ICs) is very important in many fields like defense, automotive, space communications, radio astronomy, and so on [1]. Modern phased arrays are mostly used for high-frequency applications (smaller sizes) like mm-wave 5G, 6G and many more. High frequencies offer short wavelengths, so the optimal size of individual elements is small, allowing for manufacturing compact antennas that produce sharp beams. Monitoring phased array systems during their operation is a very vital requirement for diagnostics (in case of element or IC failures, ageing, environmental changes etc.) and pattern recovery in all of the above-mentioned applications. The radiation pattern provides crucial information regarding the fundamental properties of any AUT (antenna-under-test) like the gain, beamwidth and side lobe levels. Through studying the radiation pattern, the type of antenna, amplitude, phase, gain, polarization, and various other metrics can be determined [2]. Hence, there is a need for precise characterization of the antenna radiation pattern for optimal performance of any system under consideration. Antenna diagnosis and antenna recovery (restoration of antenna array performance to its original optimal state) are two major branches of antenna array optimization. These fields are further subdivided into studies based on the near-field and far-field regions. This thesis focuses on the fast diagnosis of random antenna element failures using sparse far-field data.

(a) General phased array system **(b)** Array main beam

Figure 1.1: Phased array system [3]

1.1. Motivation

Antenna array element failure refers to the malfunction or breakdown of individual elements within an antenna array system. An antenna array typically consists of multiple elements working together to achieve specific performance characteristics, such as directional radiation patterns, beamforming, or signal reception. Especially in the case of phased arrays the complex radiators and surrounding electronics elevate the chances for faulty antenna elements. Faulty elements in large phased arrays lead to distortion in the radiation pattern and can cause changes in beamwidth, gain, and SLL (sidelobe level) [4] as illustrated in Fig. (1.2). Common challenges associated with diagnosing large phased arrays is computation time. For most practical scenarios there is a need for fast determination of faults. The initial steps involve determining the type of pattern being analyzed and assessing the stringency of the conditions imposed on the measurement setup. Hence, obtaining the desired pattern becomes the first step in satisfying the demands of the system before moving to the fault diagnosis. In conclusion, further studies using far-field patterns leads to defining more useful parameters (higher degrees of freedom)[5]. Large phased arrays are also accompanied by many challenges apart from faults, especially the IC and coupling effects [6] [7]. For phased array design, the effects of array mutual coupling loss are substantial. In practical communication and sensing systems, the loss of transmitted or received signals depends on the combination of these coupling signals and the type of radiating element [3]. Generally, once the diagnosis is done correctly, in the recovery process, the rearranging of phase and amplitude distribution of the active elements can lead to the reversal of the changes observed especially with SLL (sidelobe levels) [8].

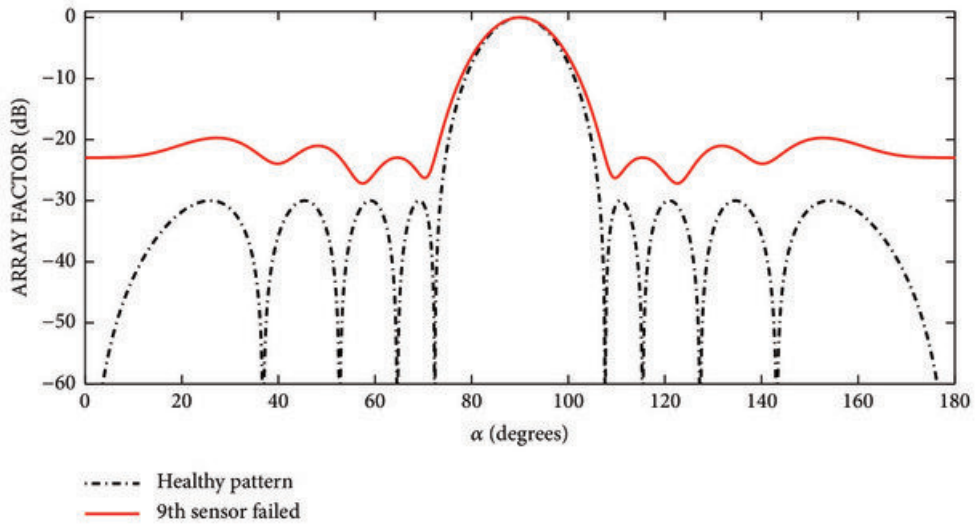

Figure 1.2: Radiation patterns of a healthy array and array with a faulty element [9]

Over-the-air (OTA) measurements of the pattern help in determining the performance of the entire array, not just for element-level failures but can be further explored for chip failures as well. The choice of type of information for such diagnosis methods is vital. The two types are near-field (curvature of signals is not negligible i.e, within the fresnel region) and far-field (the wavefront of the signal impinging on the antenna array is assumed to be a plane wave) information; the testing and identification of faults are made according to the type of information as well. Diagnosis using near-field requires time-consuming

element-by-element measurements with a moving probe. Far-field methods for measurement collection are also comparatively cheaper and faster. This thesis focuses on array element failures in phased array systems using far-field information.
Given that this is an inverse problem approach, as clearly described by Wegrowicz et al. [10], the second facet to consider is the number of measurements and sampling points. When conventional sampling methods are chosen, this utilizes a lot of time and resources for continuous array pattern monitoring. The size of measurements affects the performance greatly hence, continuous and efficient measurement collection is desired. There is a need to use sparse sampling technology for quick and efficient array diagnosis, as it helps reduce measurement time and manage a large number of measurements with fixed sampling points. The measurement setup used in this thesis motivates the study of sparse sampling points with amplitude data. As mentioned the setup under consideration also significantly reduces the time needed for scanning and obtaining the measurement samples [11], this will be discussed more in detail in this chapter.

Finally, the need for array diagnosis with modeling errors for IC-integrated arrays is a vital area of research that has yet to be explored in detail. There are many challenges like mutual coupling, chip failures, array production errors and more that need to be addressed.
This chapter delves deeper into the problem formulation, objectives, literature review, and novel contributions, laying the groundwork for the structure of the thesis.

1.2. Problem Formulation

The primary research problem addressed in this thesis is the fast determination of the number and positions of failed elements in active phased arrays. As IC-Integrated arrays bring about further non-linear and coupling effects it becomes imperative to build on the existing literature to solve the problem at hand. With limited literature on sparse non-uniform sampling and planar arrays for fault diagnosis, there is great potential to explore further large planar arrays using various metaheuristic methods and finally machine learning approaches to overcome the limitations of those methods. Many modern applications require fast determination of faults in large IC-controlled phased arrays, hence a detailed study on the design of such arrays (considering their non-linearities) and detecting these faults using deterministic, optimization or machine learning approaches is pivotal. This thesis examines the robustness of these algorithms using experimental and simulated data specific to a particular type of antenna array. More information regarding the AUT (antenna-under-test) will be mentioned in this section (1.3.1).

1.3. Measurement Setup and Scope

In this section, the measurement setup is introduced which is then followed by the scope. As the scope of the thesis is defined partially based on the key functions and limitations of the measurement setup.

1.3.1. Measurement Setup

Antenna-Under-Test (AUT)

The AUT (antenna-under-test) used for the collection of measurements is the NXP-TNO active phased array [12]. It is an 8x8 dual-polarized (H and V polarized) 5G antenna operating between 24-26 GHz

with an attached heat sink for cooling. The different cooling systems used in AESAs (active electronically steered arrays) are a wide field of study, especially in mm-wave region [13]. The core is the beamformer integrated circuits (ICs) which improves the overall performance and efficiency of each operating element (4-channel) providing the ability to focus and steer the beams on the transmit or receive end. Many of these beamformer ICs are arranged in a planar configuration to create the phased array, enhancing the system's ability to target and communicate more effectively.

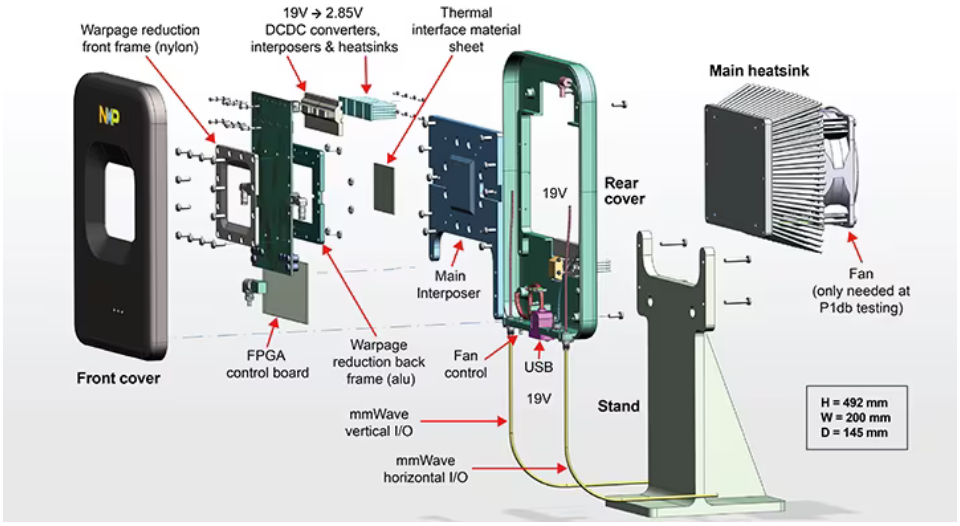

(a) Expanded view of the 5G mmWave antenna [12]

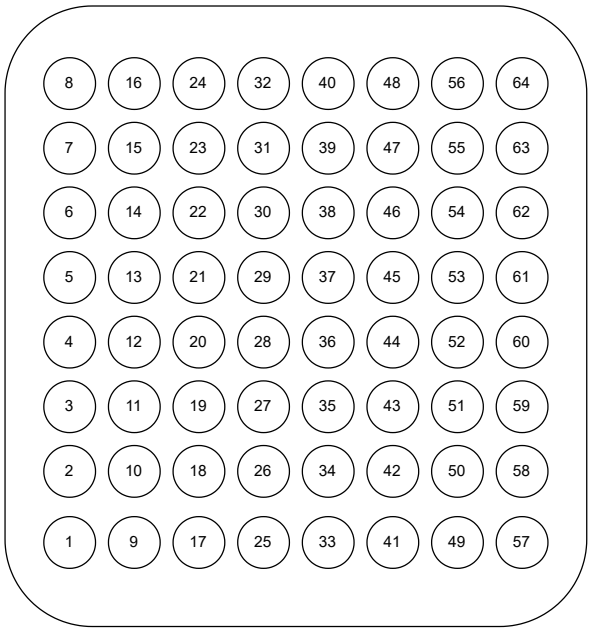

(b) Topology

Figure 1.3: Antenna-Under-Test

Initial Dome system

Antenna system characterisation has historically relied on large-scale infrastructures like anechoic chambers, achieving high accuracy at the cost of extended measurement times. Further changes made for commercial scanning equipment also rely on high-end equipment for characterisation, so the full characterisation of the antenna remains time-consuming for simple scenarios as well. The 3D array pattern acquisition setup developed at Delft university of technology (antenna dome, electronics research laboratory) removes the need for scanning equipment and heavily reduces the characterisation time (Fig .1.4).

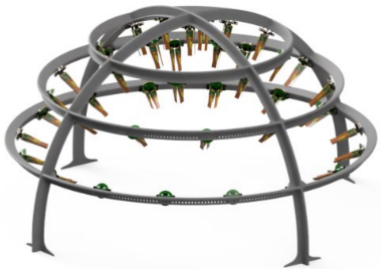

Figure 1.4: Initial Antenna Dome system (41 dual-polarized units) [14]

Recent Dome Model Innovations

The revised structure has a geodesic skeleton with dual-polarized detector cells (made up of two antipodal vivaldi antennas). The preliminary version consisted of 26 detector cells in a distributed sampling environment [11]. The latest version of this dome has 36 detector cells following the same structure (Fig. (1.5)). The broadside node and the other five nodes are placed in the center of the other hexagons making up the structure of the geodesic dome.

(a) Two antipodal vivaldi antennas used in high frequency board

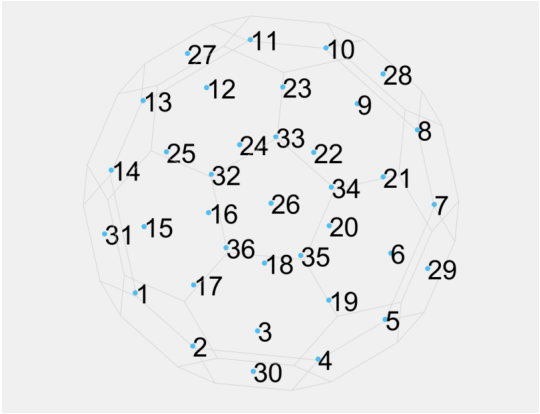

(b) Top view of the nodal configuration of the antenna dome

Figure 1.5: Antenna dome with geodesic skeleton [11]

The power measured in each node is interpolated to reconstruct the radiation pattern. Multiple correction factors are applied to mitigate the variation in each detector cell of the measurement setup. In the upcoming chapters, more studies will be conducted regarding the antenna dome's stability and improvements in scalar data collection in real-time for 5G mm-wave phased arrays.

1.3.2. Scope

Many deterministic, metaheuristic techniques and machine learning techniques are explored in the literature for a plethora of applications (as mentioned in detail in Section (1.4.2)). The AUT (antenna-under-test) and measurement setup used in this thesis are described in detail in the previous section (1.3.1). Hence, the focus is on amplitude-only data and extremely limited sampling points concerning the antenna dome [11] are chosen. This is motivated by the fact that it is a much more complex and practical challenge to use phase-less data for doing element-wise fault diagnosis. Implementing a setup or network to measure array status in real-time is both costly and requires consideration at the array's design stage. Moreover, employing phase-less data eliminates the necessity of generating a reference phase signal, which would further add complexity and expense to the system. Furthermore, the inclusion of non-linear effects, IC-controlled array errors and coupling effects fall within the scope of this project specifically as they are included in the measurement setup. The primary focus here is to analyse the practical shortcomings of the setup and compare their performances in the designed model whilst exploring regional diagnosis for multiple scenarios. There are a plethora of compensation methods that can generalise and fix all operative elements [15] in the array but this can only be done if the number and position of failed elements are known prior. As there can be variations in how an element is considered to be failed as well, scope revisions need to be done as well to include all the necessary elements in the design process. In this thesis, a comparison of the performance with the simulated and measured data is to be considered with the model (benchmark and machine learning). In this thesis, 8 random failed elements are investigated for a single frequency and polarization. Chip failures can be a nice study that comes under the scope of this project which can be investigated for more structured fails (4 neighbour elements fail).

1.4. State-of-the-Art

This chapter discusses the relevant approaches used in detecting array element failures and segregating the various methods based on the setup used in this research. This literature study summarises the relevant work done for array element failures in active phased array systems. Initially, the methods used for near-field and far-field information are discussed and then further narrowed down to methods used for far-field data specifically amplitude-only information. The inferences gained from the papers and their research gaps are briefly mentioned as well.

1.4.1. Pattern Sampling Strategies

There are mainly three categories based on the measurement distance for array diagnosis namely,

- Far-field
- Middle-field
- Near-field

Most studies on array element failures and measurement collection focus on the near-field and far-field. The following equation describes the definition of the far-field region and the variables involved.

$$R_{min} > \frac{2D^2}{\lambda} \tag{1.1}$$

Where, *D is the maximum linear dimension of the antenna* and λ is the wavelength of the EM waves.

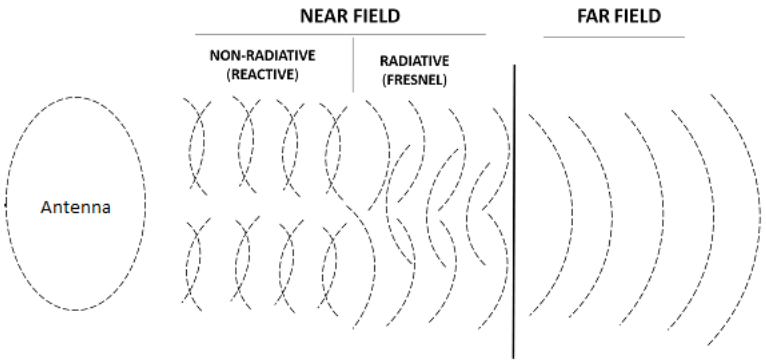

Figure 1.6: Regions of the electromagnetic field excited by an antenna [16]

But this definition does not always hold. For smaller antennas (D is comparable to λ), the R_{min} should at least be 2λ or higher to be defined as the far-field region. The near-field measurements provide large amounts of information to characterize the AUT (antenna-under-test). Commonly single probe or spherical measurement is used for studies using planar arrays. For near-field antenna measurements, a non-redundant sampling representation is described [17]. Due to the variations in sampling rate, a 2D optimal sampling interpolation is used for reconstructing the near-field on a 0.5λ grid. For the real measurements, a medium gain antenna at 11.95 GHz is collected on a planar surface (*xz*); samples are mapped from spherical to planar grid with increasing sample spacing steps from 0.5λ to 1.5λ. This strategy is concisely depicted in Fig. (1.7). The collected near-field data works well using the proposed non-redundant sampling even with a 62% decrease in sampling points. Transformation to far-field is also proposed but not with realistic parameters.

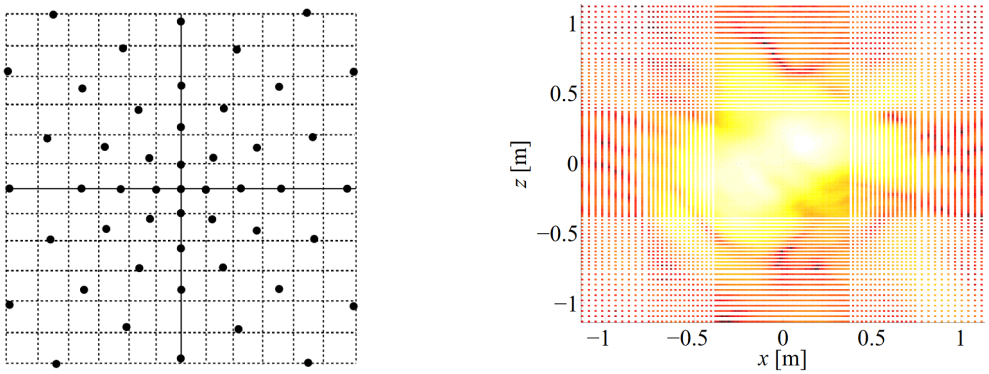

(a) Near-field sampling points on 2D planar grid

(b) Near-field distribution in dB

Figure 1.7: Near-field non-redundant sampling strategy [17]

In J.J. Lee et. al, experimental studies using an X-band finite test array which consists of 8x8 dipole elements (excited by a corporate feed network and secondly, through phase shifters) at 9.75 GHz for single-probe near-field measurements (Fig. (1.8)). Discrete points over a grid with equal spacing are chosen for sampling [18].

In all their diagnostic tests the probe distance is maintained at 5λ; probe and element corrections have been implemented to obtain better resolution. A strong quantitative study based on amplitude and phase variations in the elements is lacking and is described as future work.

A measurement setup for the NXP-TNO array (antenna-under-test (AUT) used in this thesis) with near-

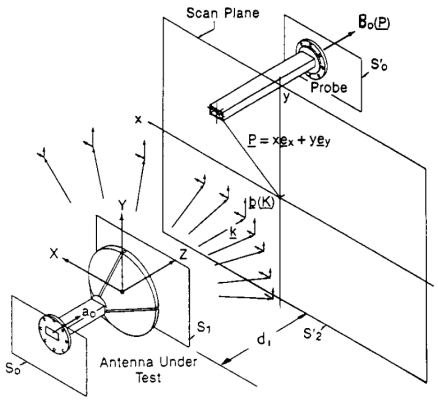

Figure 1.8: Near-field measurement strategy [18]

field sampling is described in this paper [19]. Apart from the post manufacturing calibration method mentioned in this paper, impact of measurement collection with a near-field scanner can be inferred. It is a highly time-consuming process when done element-by-element and the array pattern changes are recorded for different IC settings.

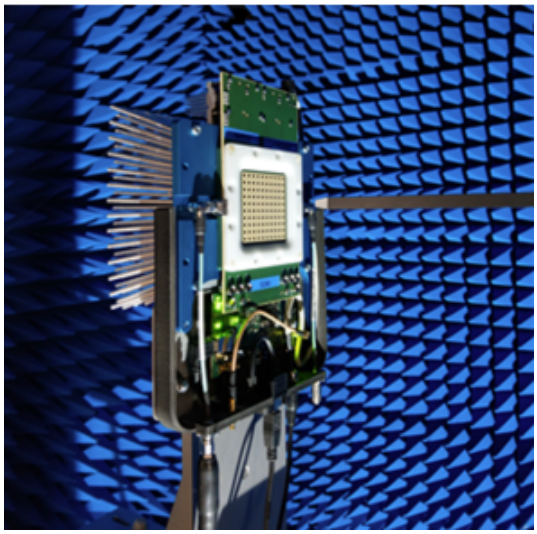

Figure 1.9: AuT in DUCAT (near-field) [19]

Studies on varying steering directions are also important for fault detection [20]. The method in this paper works well for simplified radiation configurations but is not extended to far-field cases or using realistic measurements.

Furthermore, for arrays with negligible elemental coupling, the equation for near-field patterns can be formulated easily. The number of failed elements is usually much smaller than the total number of elements in the AUT (antenna-under-test) so these elements can also be sparsely distributed in space [21]. The use of sparse information reduces the time for scanning as well. Mostly there remains the well-known trade-off between accuracy and measurement time which needs to be taken into account as this applies to any kind of information. In this paper, the focus is on using 100 uniform sampling points for reliably diagnosing failed elements using far-field data of a 64-element planar array with uniform spacing [22]. Some general reasons for using far-field data include their sensitivity to phase

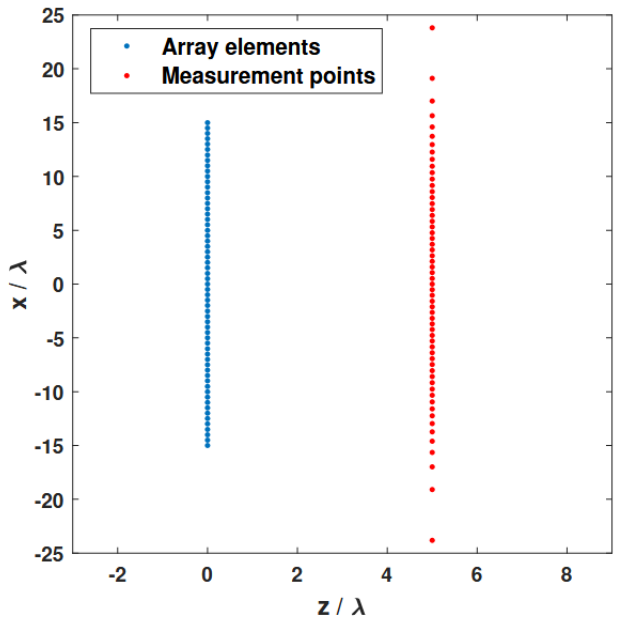

Figure 1.10: Layout and measurement points [20]

and amplitude errors compared to near-field, which require more precise instrumentation and complex analysis. Additionally, as the mm-wave frequencies are considered the far-field can be measured at a reasonable distance. Furthermore, the characterization of the far-field from near-field data requires precise probe positioning in the measurement system as described in Fig. (1.10).

Now, the discussion shifts to the dense sampling to the far-field region. The issue occurs when large measurements need to collected. For the collection of 5000 pattern data with 1° sampling in +/- 60 degree range (1D) using the NXP-TNO array including random failures take 14 hours. In this case, only the broadside beam is considered. On the other hand, the measurement collection time for a similar scenario using the dome is within 30 minutes. This further facilitates the data collection process and avoids data redundancy.

Sparse sampling helps reduce the complexity of the system. Also, provides a lot of space to explore and focus on key information which leads to better insights. It also improves the feasibility for many practical situations and makes the measurement collection process as smooth as possible. From examples in the literature, spherical configurations are used to simplify the system and can cover most angles. There are fixed distributing points or pseudo-random methods that are followed for sampling. An example of a spherical measurement array can be seen in Fig. (1.11).

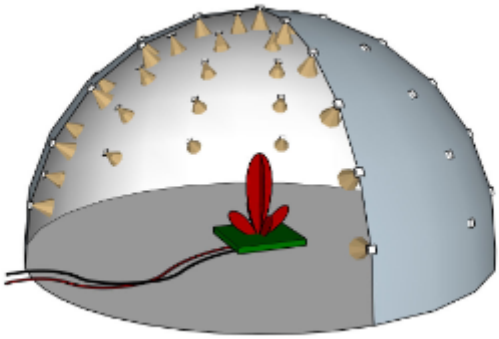

Figure 1.11: Spherical measurement setup - Fixed [23]

A more detailed description of the multi-probe measurement setup will be provided in the following section (1.3.1). The probes are present in three rings of increasing size, so it is not the conventional uniform sampling either, thus making this a more complex model to simulate and model.
Amplitude data is used for a couple of reasons, mainly:

- To avoid measuring the complex far-field pattern, which requires a reference phase signal and a highly expensive measurement setup [24];
- Reduced complexity of architecture and reduced cost;
- To complement the fast measurement setup used in this thesis, which measures amplitude-only data.

1.4.2. Fault Diagnosis Techniques

The radiation pattern is a weighted superposition equation and similarly, the adjustments according to faulty elements need to be made as well. The effect of these failures causes a significant degradation in the pattern and loss of power. The practical things that need to be kept in mind like improving the mean-time-between-failures, preserving the lifetime of T/R (transmit/receive) modules and so on are all part of rectifying the diagnosed faulty elements [25]. Multiple pattern compensation and element failure compensation techniques are widely employed to address and rectify faults in active phased arrays. Some methods also consider diagnostic problems as phase retrieval problems using few amplitude measurements [20]. With amplitude and phase data, array diagnosis is equivalent to solving a linear problem. Hence, the matrix method (MM) and back transformation methods (BTM) are used [18][26][24]. A generalization of the back transformation technique is the matrix method. They are used for most regular shaped apertures and for few faulty elements in the array. In the case of the matrix method, modified methods have been designed to obtain higher degrees of freedom and robustness to noise [27]. However, a major limitation is that it cannot be applied to array synthesis with elements at a fixed grid location. The effects of mutual coupling are also not included in the formulation of the problem.

Faster methods which utilize the computation of array factor for more search- space based algorithms. Matrix methods and backpropagation require exact excitations to synthesize the beam pattern which can be quite complex. So to capture the variability in these patterns without computing the inverse of complex matrices; also to include effects like mutual coupling, search-based/evolutionary algorithms

are more suitable. Predominantly utilized evolutionary algorithms, such as GA (genetic algorithm), PSO (particle swarm optimization), and differential evolution, are commonly employed in EM design and fault diagnosis problems, serving as robust benchmarks. In Navaamsini et.al, GA, PSO and pattern search methods are compared for 12-16 element failures [28]. This study uses an 8x8 uniform planar array (different sizes are also explored) at 100 kHz operating frequency and uses complex-valued data for fault diagnosis. Random, column, row and group fails are considered. To assess the performance SNR (signal-to-noise) values are calculated and the objective function minimizes the difference between the initial failed radiation pattern and the newly failed pattern.

$$\eta_{(\mathrm{G_p})} = 20 \log \left[\frac{\sum \mathrm{G_{BW_{3db}}}}{\sum \mathrm{G_p} - \sum \mathrm{G_{BW}ddb_{3\ d}}} \right] \tag{1.2}$$

In O.M. Bucci et.al, the diagnosis of discrete faults of a planar array for noisy far-field amplitude-only data is considered. Practical and theoretical ambiguities are considered to establish the uniqueness of the solution. A minimization-based genetic algorithm is used for the minimization problem. A few cases starting from constant amplitude and random phases over different number of generations are discussed, and the population size is maintained as 101 throughout. In this paper, an improved method for GA (genetic algorithm) which uses the far-field radiation pattern including mutual coupling effects are described [29]. The ambiguity problem is considered to be resolved. A linear array with 16 center-fed dipole antennas with 0.3λ inter-element spacing is studied including the coupling with the elements. Up to 4-fail cases are studied and validation using measurement data is carried out. For over 30 pattern samples the success rate is found, 4 failed elements with a 6/10 success rate. ANN (artificial neural networks) techniques are explored to bypass the iterative process followed by evolutionary algorithms. They also provide scope for networks driven by data for problems which are difficult to formulate.

In Patnaik et. al, linear arrays (16-element microstrip array at 1.9 GHz with 0.3λ inter-element spacing) are mainly explored but the extension to planar arrays is explained as future work [30]. A MLP (multi-layer perceptron) was trained to locate up to three faults with a training sample size of 697. These networks prove to be faster than the optimization algorithms and can be used for more versatile problems. In Fig. (1.12) shown below, the Gain (dBi) plot is shown for the single cut considered which is the ϕ = 0° plane. The intermediate and final outputs from the ANN are highlighted and the faulty element is detected. Similar plots are shown in this paper using the same plane for varying faults, which makes the differences from the non-defective radiation pattern quite evident.

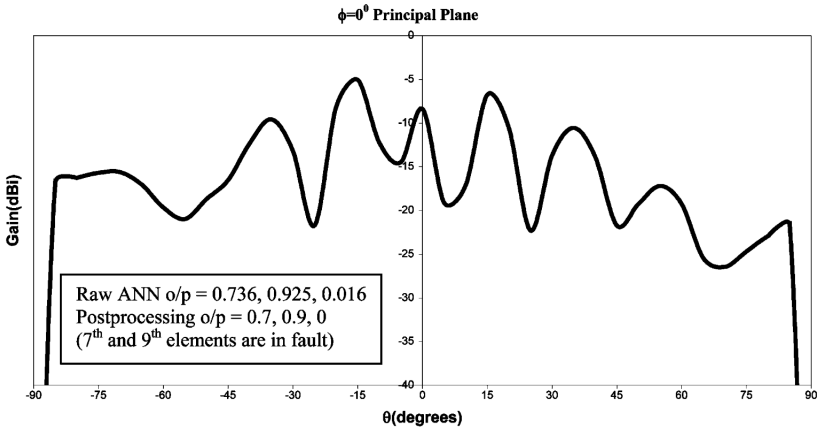

Figure 1.12: Predicted pattern with predicted element faults [30]

Some of these algorithms are also used for hyper-parameter tuning in more complex cases to improve performance [31]. The results of this combined approach are compared with a normal grid search optimized support vector machine. The antenna-under-test is a 4x4 element microstrip antenna array with a corporate feed network. For the study of complex-valued data and diagnosis of up to three faults, the proposed method takes 381 seconds with complete accuracy for three faults.

In Yao et al. a similar setup is described with the design of a 3x3 patch array in MATLAB with mutual coupling included [32]. For single-unit failures, the method using a deep convolutional network in MATLAB is shown to have a high success rate. The comparison is done with practical scenarios where extreme conditions are exposed to the antenna array. Noise level is maintained at signal-to-noise (SNR) = 5dB for most cases.
The received far-field radiation pattern is transformed into the prediction of the faulty units in the antenna array. The full wave simulated data from CST Microwave studio of a 3x3 planar antenna array is used as the input 'image' matrix (complex-valued) with some added gaussian noise (SNR = 5dB) and the faulty units as output. This method is data-driven and does not require the computation of Green's function. The use of hybrid methods like combining the optimizer and ML leads to a good increase in diagnosis time. Similarly, the effectiveness is highly improved whilst using machine learning techniques as it only requires one-time far-field simulation or measurement. The space in which the antenna-under-test is used can be modified by retraining the network and does not require complex reformulation. The non-linearities and other challenges from IC-controlled arrays can be included directly without iteratively computing large matrices.

A comprehensive table illustrates the key literature for the various fault diagnosis techniques, providing proper perspective and direction for this thesis (Table .1.1).

Papers	Approach	Array Setting	Data type	Number of faults	Freq. of Operation	Sampling and Measurement points	Weaknesses
[33]	Discrete Search space, Binary coded genetic algorithm.	Uniform Planar array, increasing up to (20x20)	Amplitude-Only data	On-off Faults, for possible (2,3,4) faulty elements.	-	Cardinality of population is kept as 101.	Ambiguity problem is intrinsically less relevant. Use of Array factor data and uniformly distributed noise.
[30]	ANN is used to do the mapping from distorted radiation pattern to the output vector including mutual coupling.	Linear Microstrip Antenna (16 element, 1512 mil x 1500 mil element size, 0.3λ spacing)	Gain pattern in principle plane ($\phi = 0°$)	Maximum 3 On-Off faults	1.9 GHz	37 sampling points and 697 measurement samples for training.	Only linear array case is considered. Requires a lot of information to prevent over-fitting, and simple post-processing for a small number of faults.
[24]	Mixed l1/l2 norm compared with BPA and MMA	10x10 open-ended waveguide array	Complex valued and Amplitude only data	Important and medium failures are defined with variations in phase and amplitude.	12 GHz	1000 measurement points with 150 sampling points.	Complex setup, Best performance only with good priori information (Fault-free array information).
[31]	CNN used with Genetic algorithm is compared with grid-based search and Support vector machine	4x4 Planar microstrip antenna array	Complex-valued data	1-3 On-Off faults	3300 - 3670 MHz	374-1078 measurements	Small sample set, only full-wave simulated data is considered with less number of faults.
[28]	GA, PSO and simulated annealing are compared. Spatial signal processing.	8x8 uniform planar array using phased array beamforming method.	Complex-valued data	12-16 element failures	100 KHz	Varying based on antenna size	Does not include highly non-linear effects. Phase information is essential.

Table 1.1: Comparison of various fault diagnosis approaches in phased arrays

1.4.3. Conclusions

The above conducted literature study is partitioned into two major sections which resulted in some conclusions considering the problem tackled in this thesis. Essentially, the aim is to achieve diagnosis in almost real-time for practical arrays which include IC non-linearities and mutual coupling effects. In the existing literature, the focus primarily revolves around complex data in the far-field region, employing a range of techniques such as beam pattern synthesis, pattern reconstruction, and inverse problem methods.

- The deterministic methods include Matrix Pencil, Backpropagation and so on. Although they are fast methods, they require an accurate formulation of the problem and do not include the non-linearities involved in a practical system.
- For different heuristic approaches like evolutionary algorithms (GA, PSO, PS, etc.), convex optimization and so on. There are many methods explored for ideal linear and planar arrays but does not include IC non-linearities. Mutual coupling is included in some papers. GA - like algorithms are chosen as they fit well with the binary nature of the unknowns and can be explored further.
- Machine learning algorithms lead to real-time diagnosis solutions. However, most of the papers deal with full-wave simulated data and densely sampled far-field data for linear or small planar arrays in ideal conditions.

From the literature, it can be seen that the various non-linear changes in each IC channel response (temperature variations, load pull effects, etc.) in large-sized arrays integrated with sparse pattern sampling have not been studied till now. The literature does not have a specific comparison benchmark for faulty diagnosis of 2D active phased arrays (including IC non-linearities and coupling effects) using a fast measurement collection setup for compliance with in-field operation. Based on the findings from the literature review, the research objectives have been formulated (mentioned in detail in the next section (1.5)).

1.5. Objectives

Based on the research problem and literature study conducted on fault diagnosis methods and various measurement strategies the following research objectives can be formulated.
The Master Thesis aims to,

- Identify the relation between the field strength variations at the sparse pattern sampling points and the location of the failed elements or ICs.
- Develop and assess the performance of a benchmark optimizer based on the array factor theory for the detection of randomly failed array elements.
- Propose a novel machine-learning framework for the same purpose, including the IC (integrated-circuit) non-linearities and mutual coupling.
- Demonstrate and compare the performance of the proposed technique to the benchmark. Comparison studies using the proposed technique using simulated measured data are to be conducted.

1.6. Novel Contributions

This thesis proposes a novel use of amplitude-only sparse far-field sampled data for array element failure diagnosis allowing for fast real-time failure detection using ML-assisted techniques. The superiority of these techniques over evolutionary optimization is to be established. The effects of PA loading, feeding inaccuracies and mutual coupling are taken into account for the first time in designing the model for solving this inverse problem. The measurement setup (sparse) provides additional benefits such as fast and numerous measurements with a fixed number of sampling points. Regional diagnosis in both the array and the sampling regions is studied, and initial analyses are conducted. This helps in understanding the behaviour and importance of the far sidelobes in such applications.

1.7. Thesis Structure

The remainder of the thesis is organized as follows. In Chapter 2, the theory behind the array pattern simulations are discussed along with motivating the use of metaheuristic methods. It also includes deterministic and statistical analysis studies for Patch Antenna Array element failures. In Chapter 3, a discussion regarding the methodology followed for the benchmark studies and the motivation for using machine learning methods is presented. Full-wave simulated data is also introduced in detail. In Chapter 4, the methodology for the machine learning method is introduced along with a brief understanding of the measurement data. In Chapter 5, a comprehensive comparison between the GA and ML methods are conducted for varying number of faults and sampling points. Finally, in Chapter 6, the final results are summarized and the meaningful conclusions drawn from the study are described.

2

Pattern Formation Under Element Failures

This chapter begins with an overview of the fundamental principles and initial expressions related to radiation pattern generation. This is followed by studies using simulated data to identify algorithms well-suited for diagnosing faults in antenna arrays. These studies entail some deterministic and random scenarios for fault diagnosis which help in motivating the use of more complex methods further.

2.1. Sampling with the Antenna Dome

The array pattern can be found using the pattern multiplication method where the element pattern is multiplied by the array factor (AF) but this is in the ideal case under the linearity assumption.
The radiation pattern depicts the gain or directivity over a sphere. Mostly in theta-phi or Azimuth-Elevation planes. They can also be depicted using their cosine formulation using the u-v coordinates (2D Orthographic). The far-field equation is described as follows,

$$FF(\theta,\phi) = \sum_{n=1}^{N} E_n(\theta,\phi) w_n e^{jk(x_n \sin\theta \cos\phi + y_n \sin\theta \sin\phi)} \tag{2.1}$$

Parameters	Explanation
$E_n(\theta,\phi)$	EEP of n-th element.
λ	Wavelength at the operating frequency.
x_n and y_n	X-Y coordinate element positions.
k	Wavenumber, $k = 2\pi/\lambda$
w_n	Complex excitation coefficient

In the scope of this thesis, only broadside radiation pattern investigation is carried out. Hence, no phase difference between elements or beam scanning is considered. In this chapter, instead of the EEP ($E_n(\theta,\phi)$), the isolated element pattern of a Patch antenna is chosen to approximate the antenna pattern in the AUT (antenna-under-test).

The studies conducted involve the behaviour of sparse sampling points after mapping them to the radiation pattern. As described in detail in section (1.3.1), there are 36 sparsely distributed sampling points on the hemisphere which represent the nodes from the antenna dome, using which each point can be characterized from the array pattern/far-field pattern. The primary drawback of using this measurement system is that if a node is positioned at a null in the radiation pattern, it cannot capture any information. Conversely, the center node, which captures most of the radiation from the main beam, can significantly influence the measurements. Therefore, strategically selecting specific nodes for diagnosis is crucial for obtaining accurate results.
The ideal array pattern without faulty elements is represented using uv-coordinates which are derived from the (θ,ϕ) angles (Fig. (2.1)). Their relations are described below,

$$u = \sin\theta\cos\phi, v = \sin\theta\sin\phi$$

To map the 36 points from the antenna dome (section (1.3.1)) the relations between the used and conventional coordinate systems need to be understood [34]. Therefore, the following set of relations will assist in converting the (θ,ϕ) angles from the measurement setup to the uv-coordinates of the generated array pattern.

$$\begin{aligned} x = R\sin(\theta)\cos(\phi), \quad y = R\sin(\theta)\sin(\phi), \quad z = R\cos(\theta), \\ \varphi_{\text{az}} = \arctan(x/z) = \arctan(\tan(\theta)\cos(\phi)), \\ \varphi_{\text{el}} = \arctan(y/z) = \arctan(\tan(\theta)\sin(\phi)), \\ \phi = \arctan\left(\tan\left(\varphi_{\text{el}}\right) / \tan\left(\varphi_{\text{az}}\right)\right), \\ \theta = \arctan\left(\sqrt{\tan\left(\varphi_{\text{el}}\right)^2 + \tan\left(\varphi_{\text{az}}\right)^2}\right). \end{aligned} \tag{2.2}$$

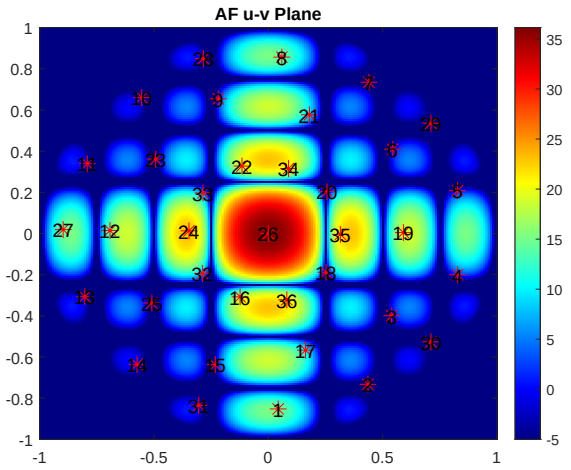

Figure 2.1: Original Pattern (No faults)

2.2. Deterministic Fail Scenarios

Based on the position of faults in the antenna array, there are drastic changes in the radiation pattern. These changes can be partially detected using deterministic methods, especially in the case of multi-channel IC failure that results in regional multi-element fails.. As deterministic scenarios provide a controlled environment to study the behaviour of structured faults, their effect on antenna performance can be analyzed systematically. They also provide a baseline for more complex, random failures leading to a more efficient testing process. In practical scenarios, a channel failure in the antenna-under-test (AUT) affects four antenna elements connected to a single channel, resulting in their deactivation. Consequently, the problem of managing 64 individual elements can be simplified to dealing with a sub-array of 16 channels. However, the focus is still on keeping the problem at the element level with random fail scenarios. Throughout this thesis, the number of faults considered will be 8 as the approach is to make the simulated scenarios as close to practical cases as possible. Starting with three broad scenarios with center, edge and corner faults which are depicted in the upcoming plots. In this chapter, the word 'ring' will be used to denote the three layers of detector cells in the Dome setup, this does not relate to the old dome model. It is only used as a means to easily describe the results. Fig. (2.2) represents the topology and array pattern with 8 center faults.

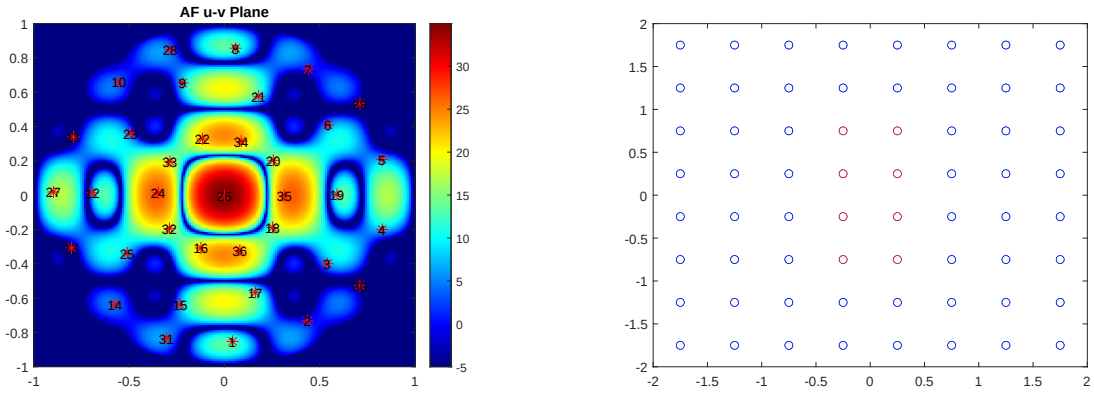

(a) Array Pattern with 8 Center faults

(b) Topology - Center faults

Figure 2.2: Center faults Array pattern - Broadside (8x8)

In the center case, it can be seen that there are some notable perturbations in the pattern. There is a significant increase in surrounding sidelobe levels and the direct impact of the center fails can be seen. They create stronger sidelobes surrounding the main beam and some unexpected nulls in the far sidelobe region. Overall directivity loss is 1.17 dB relative to the ideal pattern. Fig. (2.3) describes the edge faults case,

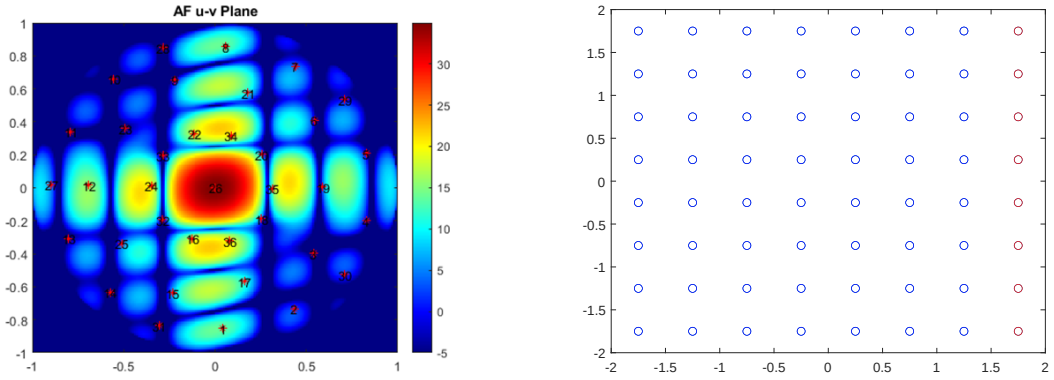

(a) Array Pattern with 8 Edge faults

(b) Topology - Edge faults

Figure 2.3: Edge faults Array pattern - Broadside(8x8)

In the edge case, there is no significant increase in sidelobe levels like in the center scenario. However, slight alterations in the sidelobe levels are evident along the region of faults With an increase in the number of far sidelobes, which leads to interesting discussions regarding the sampling points further in the chapter.

Lastly, the corner fault patterns with the respective topology are shown in Fig. (2.4). There are notable changes in the far sidelobes, both in terms of their number and an increase in their gain. The pattern still remains symmetric with the perturbations, similar to the edge and center cases. Such re-distributions led to 1.1 dB loss relative to the ideal pattern. This suggests that the recovery of such structured elements is simpler compared to random failures throughout the array [35].

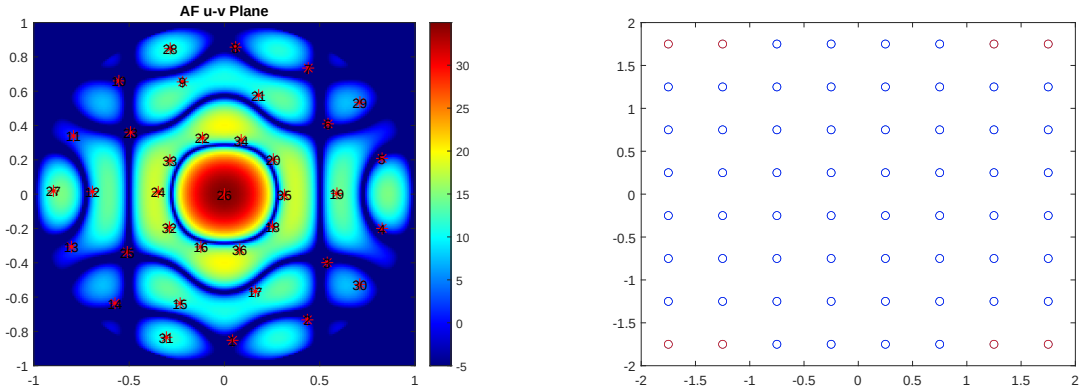

(a) Array Pattern with 8 Corner faults

(b) Topology - Corner faults

Figure 2.4: Corner faults Array pattern (8x8)

2.2.1. Studies on Fails at Center-Edge-Corner regions

This deterministic study is carried out when there is no shift in the position of the array whilst considering the aforementioned scenarios with center, edge and corner fails. For example, the points in the array around the edge have a different surrounding environment against elements in the middle and hence behave differently. This makes an even larger difference when effects like mutual coupling are

considered which will be discussed further. The values have been normalized to 0 dB to offer a clear perspective on the impact of each point concerning the difference in sidelobe levels. The highlighted points represent the cases with relatively the highest variation in the absolute SLL value in dB, the inference being these points belong to the outer ring of the Antenna Dome structure Fig. (2.5). As highlighted in the previous section (2.2), the far sidelobe variation is quite significant in all three cases albeit with varying changes. Hence, the outer detector cells capture these variations hence, carry useful information.

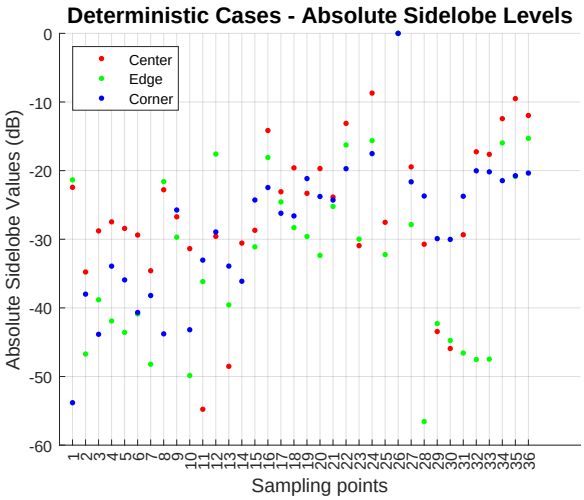

Figure 2.5: Absolute Sidelobe Levels - Deterministic Case (No Shift)

Important conclusions from deterministic faults,

- Center faults tend to have higher sidelobe levels more concentrated in the -30 dB to -20 dB area which indicates a significant impact on the array pattern and redistribution of power.
- Edge faults tend to have lower SLL values relative to the center faults, maintaining the region -40 dB to -30 dB.
- Corner faults have very less impact on the sidelobe levels compared to its former counterparts often results in values lower than or around -40 dB.

Through this, an important takeaway is that with deterministic fails in three different regions, each failed region has a different effect on the sampling points and sidelobe level distribution. The impact of each sampling point is an important aspect which needs to be quantified to increase the degrees of freedom, with more points being used for the fault detection process. This is assessed in detail in the upcoming section using standard deviation plots (2.9a).

Studies on Center-Edge-Corner with XY Shift

The position of the array also affects the detector cells/units that prove to be significant and deliver useful information. In Fig.(2.7), it is evident that the points capture different parts of the array pattern. The main beam gain value is no longer captured by the 26th Dome sampling point but is shifted according to the Dome coordinates. To visualize this XY shift more easily, Fig. (2.6) illustrates an example of a diagonal shift in the antenna array whereas the measurement setup (antenna dome) remains intact. This is not an exact illustration of the measurement setup or the shift analyzed in this chapter.

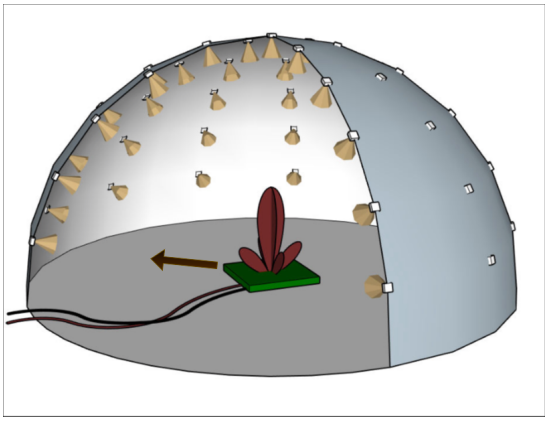

Figure 2.6: XY Shift visualization

The topology describes how the shift occurs and the various changes that can be captured.

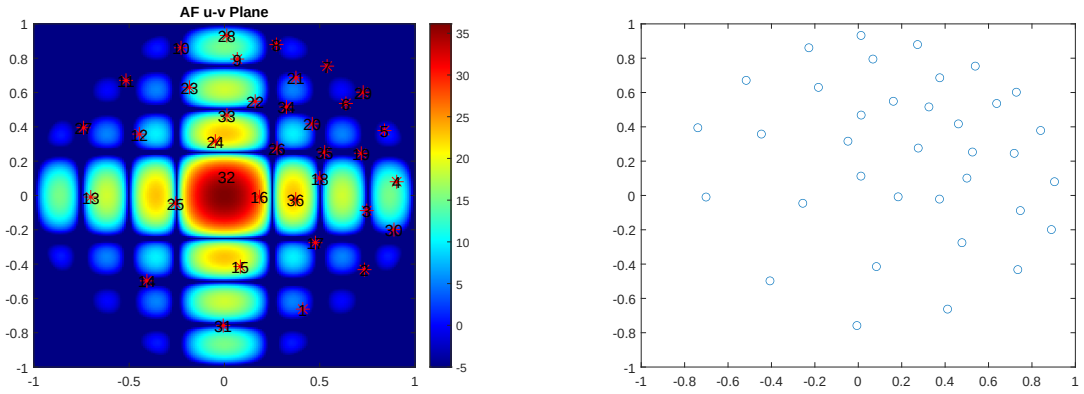

(a) Array Pattern with XY shift

(b) Topology - XY Shift [+0.3, +0.3]

Figure 2.7: Pattern with XY shift

The discussion involving the changes in the pattern for the 3 different fails leads to some interesting results. The 33rd sampling point is the one closest to capturing the main beam (in dB) and the rest of the sampling points carry different levels of information. It is observed now that the outermost ring and the innermost ring carry the most information. Hence, it can also be inferred that the main sidelobes and far sidelobes hold the most useful information. The differences are calculated between the 3 cases and do not concern the ideal scenario. The main reasons for doing this kind of comparison,

- The absolute SLL value for the ideal value contains very low values for specific sampling points and creates an unwanted weightage in some cases.
- So, the absolute SLL is considered without the reference pattern (ideal).
- The difference/range between the 3 scenarios (essentially different types of faults) is more useful to this problem in comparison to it's behaviour with the reference pattern.

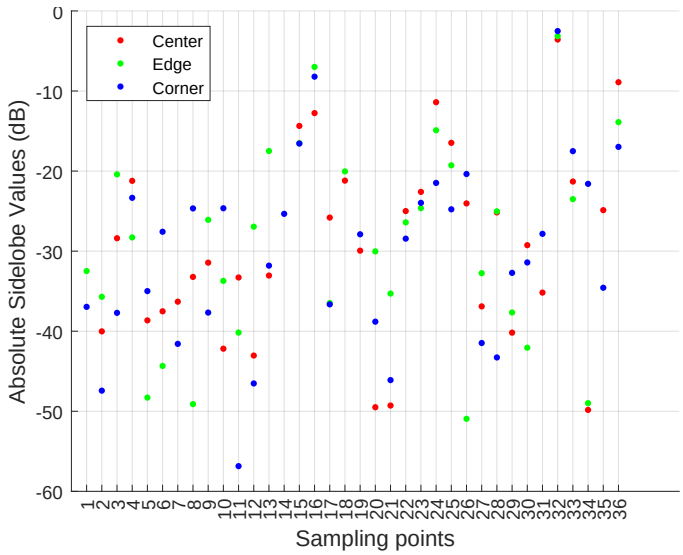

Figure 2.8: Absolute Sidelobe Levels - Deterministic Case (XY Shift)

To assess the amount of valuable information held by the different sampling points, the standard deviation is calculated for these 3 cases for No shift and XY shift (Fig. (2.9),

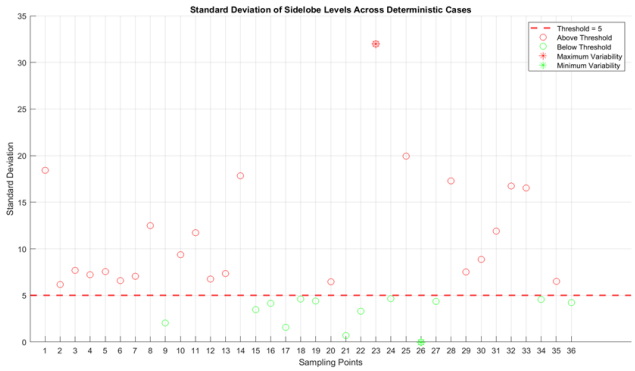

(a) Standard Deviation with No Shift

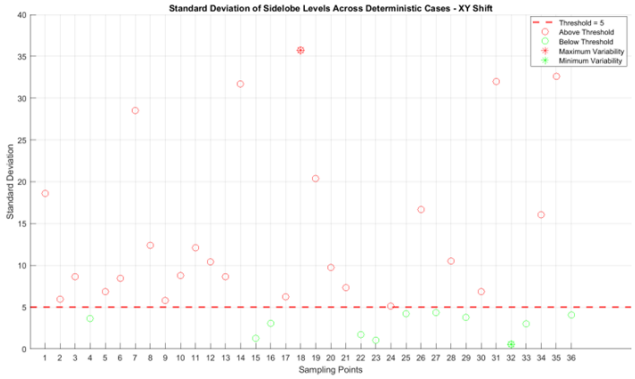

(b) Standard Deviation - XY Shift

Figure 2.9: Standard Deviation Plots

From these plots, it can be seen that in the No shift scenario, there are 20 sampling points which carry useful information as they are present above the assigned threshold. This threshold was selected based on the median of the standard deviation values. In the XY Shift case, there are 26 sampling points which are present above the threshold hence, more points can be used to obtain useful information in this case. A higher number of sampling points are found to be useful with the XY shift. Another important inference from this observation is that with more number of sampling points with useful information, it improves the degrees of freedom whilst using more complex methods like optimizers and so on.

2.2.2. Studies on Fails at Hybrid Regions

Quite similar to the previous subsection (2.2.1), the mixed combinations of the edge-center-corner are plotted. There are significantly lesser SLL values to highlight specific rings of the dome as it follows the characteristics of both types of fails. In Fig. (2.10), for example, the edge-center case follows the trend of both these kinds of faults but the prominent differences in sidelobe levels seem to be averaged. So the magnitude of difference is no longer the same as the separately considered faults scenario. It is difficult in this case to arrive at the conclusion in which region there is the most significant change.

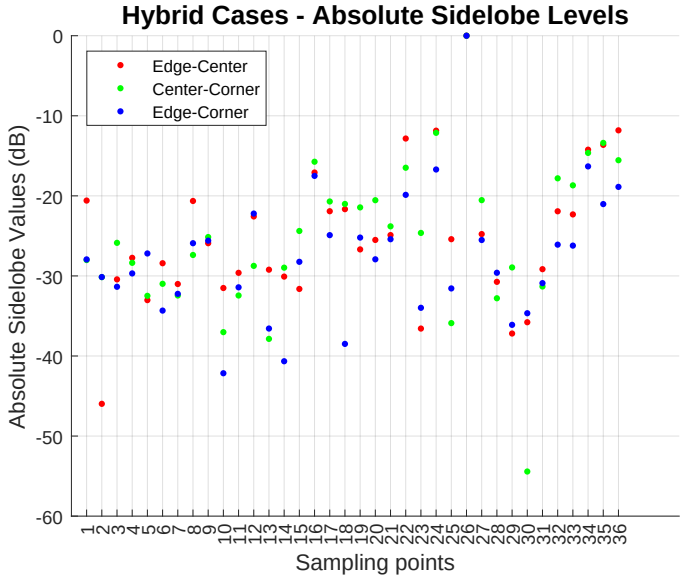

Figure 2.10: Absolute Sidelobe Levels - Hybrid Case (No Shift)

Hybrid Scenarios with XY Shift

This study includes the hybrid cases with the XY shift (Fig. (2.11)). From relatively calculating the difference between the three cases, it can be inferred that the inner ring carries the most information. So the highlighted sampling points carry more weightage compared to the others. An important inference from this plot is that indeed it does follow the trends of the original edge-center-corner cases but it does not contain as much information as contained when it was just the center case and so on.

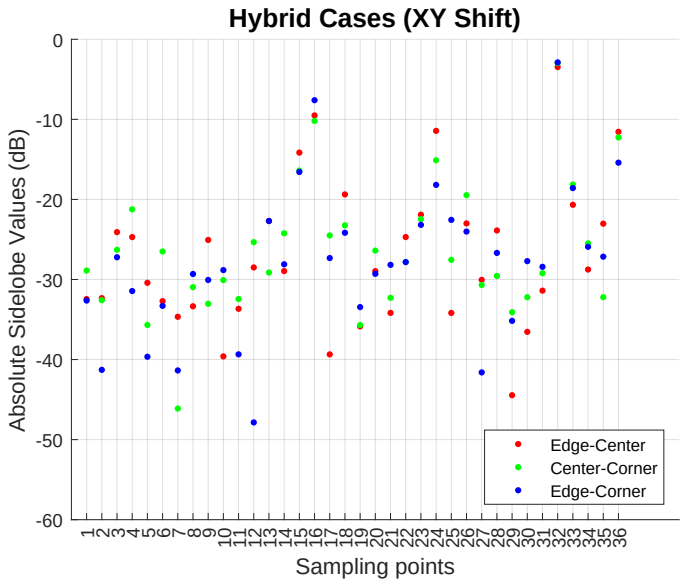

Figure 2.11: Absolute Sidelobe Levels - Hybrid Case (XY Shift)

2.3. Random Fail (Statistical) Scenarios

Apart from the complete IC (integrated-circuits) failures that lead to regional fails, it is common to have random IC channel failures that lead to failed elements at random positions in the phased array. Therefore, a statistical study of 8 random faults with 100 realizations is considered. Their array pattern values are collected from the mapped sampling points. To understand if discernible patterns can be obtained from studying the random cases.

No Shift

The results from generating 100 cases of random 8 fails are shown in Fig. (2.12a). There is a significant spread of variability across these sampling points some trends can be seen but unlike the deterministic fail scenarios, it is not easy to detect the region of failed elements. Discovering trends for specific regions or element failures is quite difficult to determine due to randomness. Some sampling points show higher concentrations of higher SLL values, for example, (1,2,4,11,29,33-36). Here, it can be inferred that they contribute less significant information statistically over 100 random fails. The overlapping data points and high variability do not indicate easily identifiable patterns in the sidelobe levels at each sampling point. Hence, the a need for optimizers which systematically reduce the variability in SLL and converge to stable solutions. Also as the generation of AF data is very practical for creating the candidate solution set it makes the fault detection process also scalable.

XY Shift

The results from generating 100 cases of random 8 fails with XY shift (similar to the No Shift scenarios) considered are depicted in Fig. (2.12b). There is still high variability and numerous outliers (mainly below -40 dB). Most deviations are observed below the lower quartile. The priority here is to categorize valuable points to catch faults early even if it is not possible through simple methods. There are more points with high variability in comparison to the No Shift scenario concerning their Interquartile ranges.

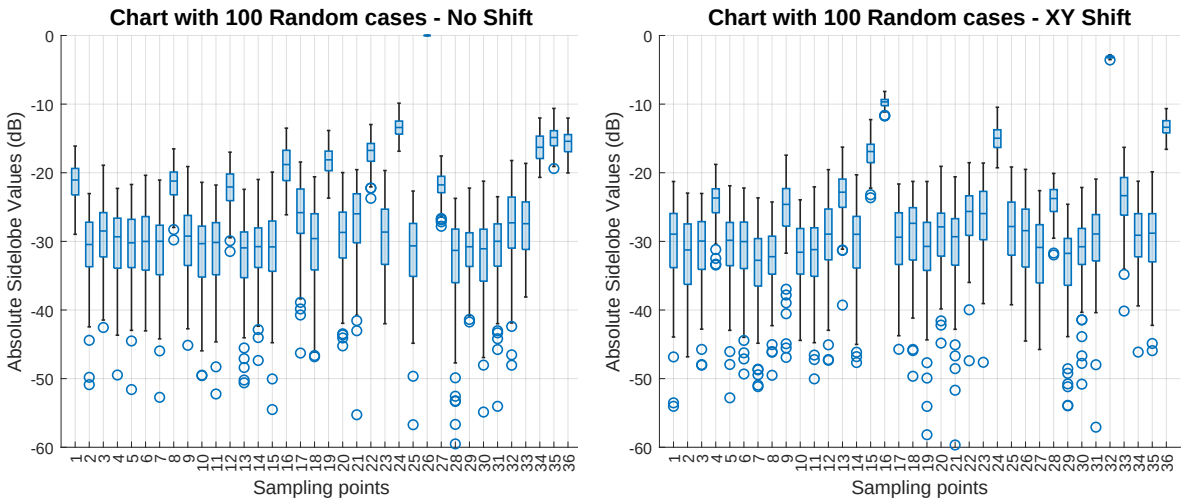

(a) Absolute Sidelobe Levels - Random Case (No Shift)

(b) Absolute Sidelobe Levels - Random Case (XY Shift)

Figure 2.12: Pattern with No shift and XY shift with 8 failures

2.4. Conclusions

The major conclusions from the chapter are that center fails has the most impact on the sidelobe levels and power redistribution. Edge fails have slight changes but maintain the overall pattern. There is pattern distortion in the case of corner faults but has the least directivity loss. The importance of each sampling point is assessed using statistical analysis and random fail cases. Firstly, from this chapter, it can be seen that for IC (integrated-circuit) failures with regional diagnosis, it may be possible to use deterministic studies. However, in case of hybrid regional fails or random element fails, just observing the patterns is not sufficient and there is a need for optimizers that understand the variations in the pattern and detect the position of the failed elements. Furthermore, there are some sampling points which relatively carry more information. This is a very interesting point to work on in the future to assign weights/significance to the points based on the information they carry. In this thesis, all the 36 sampling points are used.

3

Heuristic approach

3.1. Data Generation

Before introducing the benchmark algorithm and delving into the approach, the different types of data studied in this thesis are described here. The current and following chapters use the data described here and comparison studies are carried out between the benchmark and the machine-learning method.

3.1.1. Simulated Data

To bring about results comparable to the practical scenario, non-linear effects like mutual coupling must be incorporated into the simulated data. In this section, a brief description of acquiring this data using the CST Microwave Studio is mentioned. There are two types of data considered in this thesis which are generated using simulations, the final category is the measured data which will be described in this section (3.1.2). First is Array factor data where isolated patterns are used without mutual coupling or any other array effects. Secondly, the full-wave simulated data is generated (with mutual coupling effects) using CST Microwave Studio and is exported for further analyses.
CST Microwave Studio is a comprehensive simulation tool for high-frequency simulation to carry out electromagnetic analyses and design. It is equipped with both frequency and time domain solvers, allowing for simultaneous excitations. It supports single-element and array-based simulations. The frequency domain solver employs the finite element method for various port types or simultaneous port calculations. It is advantageous to use this method for narrow-band scenarios or unstructured meshes compared to other solvers. The time domain solver integrates the finite integration technique and transmission line matrix for 3D full-wave simulations hence known for providing the largest simulation flexibility. It is highly efficient for high-frequency applications like connectors, antennas, waveguides and so on. An array is created by modeling a single element and then expanding it with appropriate inter-element spacing. The simulation setup used in this study is an 8x8 pin-fed patch antenna array. The aperture size is 3.5λ x 3.5λ. Lossy materials are used in this design. The following figures (Fig. (3.2) - Fig. (3.1)) describe the orientation, design and embedded element pattern.

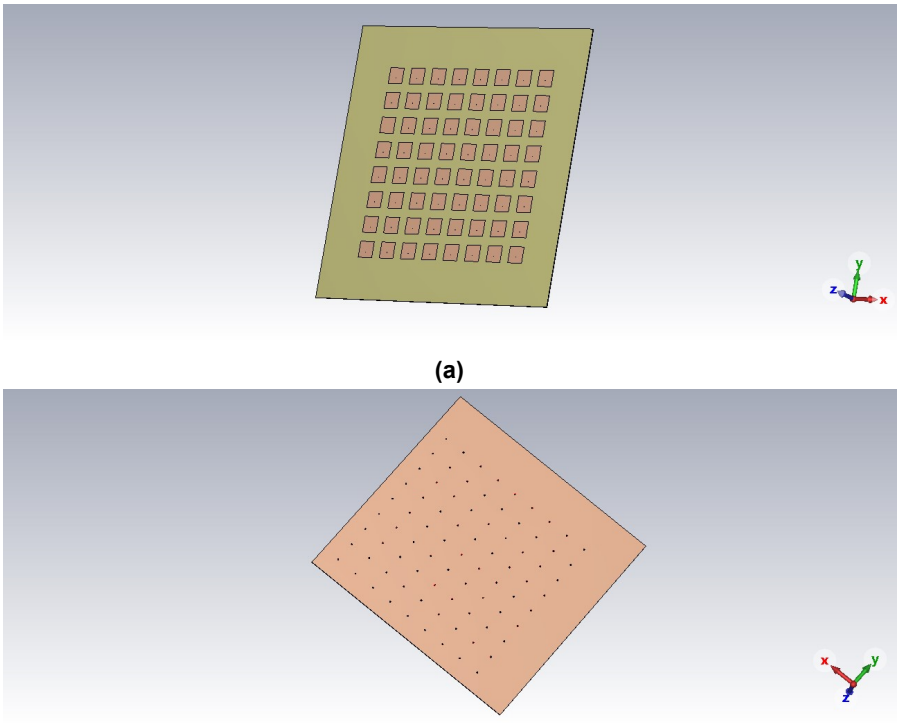

(a)

(b)

Figure 3.1: 8x8 pin-fed patch antenna array

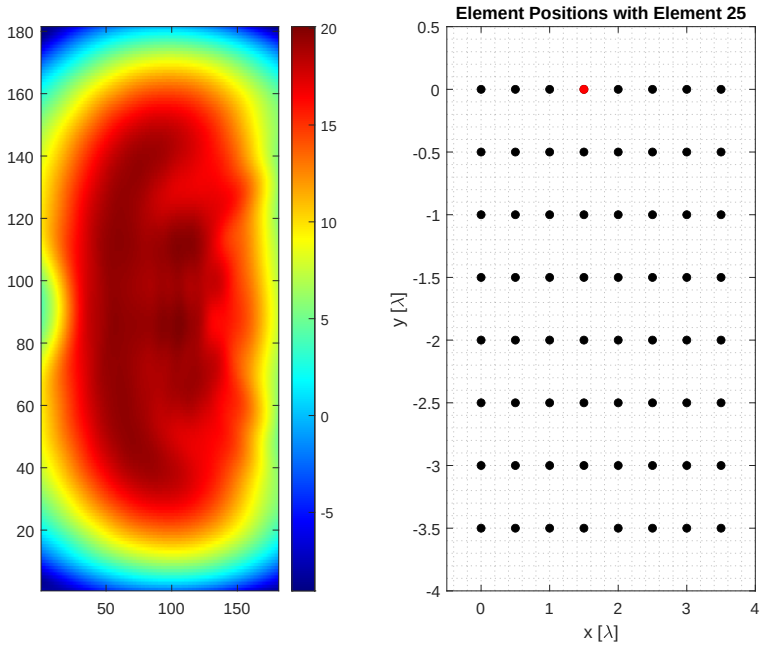

Figure 3.2: Single EEP (25th Element)

In CST, EEPs (embedded element patterns) are found by exciting the ports sequentially. These results are extracted for further processing in MATLAB. The EEPs are exported in the (θ, ϕ) plane. So, to generate the complete far-field pattern the obtained EEPs are used instead of the IEP of the patch

antenna array.

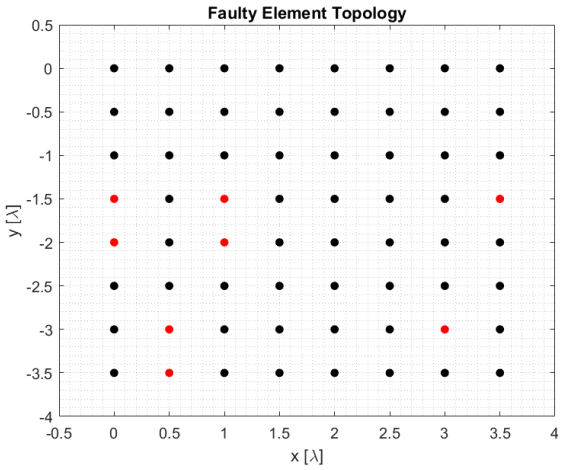

Figure 3.3: Faulty Element topology (8 faults) for UV plots in Fig. (3.4)

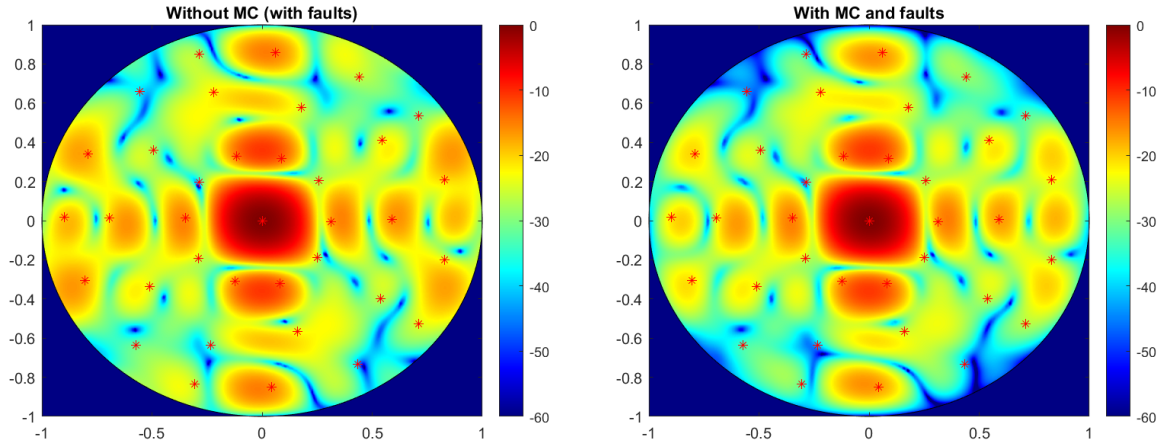

(a) UV plot with chosen faulty topology (without MC)

(b) UV plot with MC and chosen faulty topology

Figure 3.4: UV plots of fault patterns with and without MC (8 faults)

The aim is indeed to discern the number and position of faults in the antenna array, so by studying how close the full-wave simulated pattern is to the far-field pattern without MC is an important metric. However, this will not completely converge to zero (with current parameters) as the far-field pattern contains the EEP which has MC effects.

A noise e is introduced in this data as well to bring it as close as possible to the measured data. To check the performance of the network different levels of noise were tried but in general, the following parameters were used for generating the noise to include the real-time errors.

The value of e is provided for an SNR value of 5 dB,

$$e = \frac{\mathcal{N}(0,1)}{\sqrt{2}} \max\left(FF\right)\left(0.5623\right) \tag{3.1}$$

where $\mathcal{N}(0,1)$ is a random Gaussian distribution vector with zero mean and standard deviation of 1.

3.1.2. Measured data

The measured values for this thesis are collected from the antenna dome measurement setup using the NXP-TNO phased array as the antenna-under-test. The operating frequency is 26 GHz. The measurement setup allows for fast measurement collection. An overview of the laboratory setup is described here as an extension to this section (1.3.1).

Figure 3.5: Dome measurement setup

A closer view of the antenna-under-test and the detector cells within the dome structure is shown in Fig. (3.6).

(a) AUT and cooling system **(b)** Inside view of dome structure

Figure 3.6: Measurement setup for data collection (ELCA)

The general steps followed for the collection of data measurements are as follows. The AUT (antenna-under-test) is connected to the RF source with 0 dBm and the frequency is set to 26 GHz. Then after initializing the detector cells within the dome structure, the array is initialized using the NXP software interface which shows all the working channels and the temperature sensor values. Finally, using MATLAB a code is prepared to randomly fail 8 elements in the antenna-under-test and collect the required 5000 measurements. Also, later on, more data will be collected for improving the accuracy of the model.
The following block diagram (Fig. (3.7)) briefly introduces the measured data and the different non-linearities which can be quantified for it,

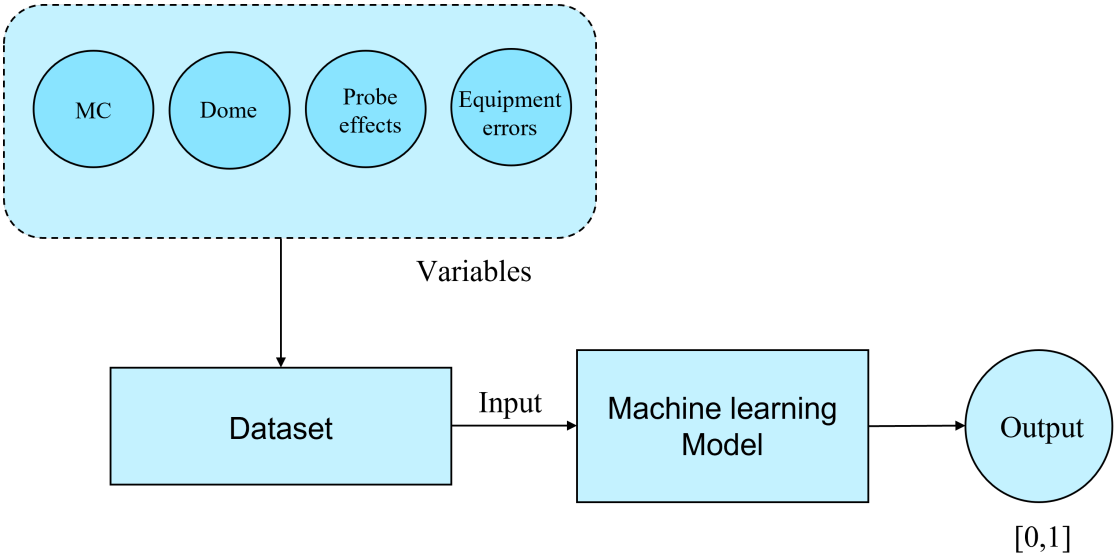

Figure 3.7: Measured data description

The first component here is the Mutual coupling which is part of the sensor values obtained from the detector cells as the AUT (antenna-under-test) especially is known to have quite high mutual coupling. This has been included with the EEPs (embedded element pattern) as part of the simulated data but it is hard to accurately describe the practical MC (mutual coupling) values in terms of a coupling matrix to the network. Along with the upcoming components, it further motivates the use of a data-driven model. The second component is effects from the Dome setup itself. Upon inspection of the measurements there was a transient found due to the time delay between the AUT (antenna-under-test) and the Dome setup. This transient was present within the first few measurements taken as shown in the figure (3.8),

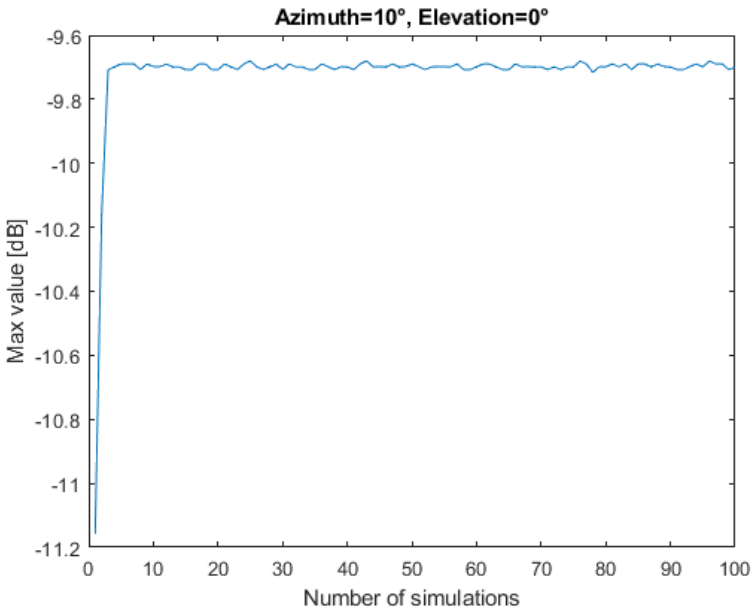

Figure 3.8: Transient in Measurements

It can be seen that the transient is present as part of the first few measurements (10-12) and then stabilises to provide consistent values. This is a part of the preprocessing where the first few measurements are removed to prevent the negative effects of this transient. Further studies were conducted to understand the stability of the Dome and how the measurement collection can be done. The beam scanning capability of the dome is quite clear till 45° range but this could also be because of the AUT (antenna-under-test) which is also known to have strong MC (mutual coupling) effects. So these limitations prevail when beam scanning is considered but in this thesis, only the broadside measurements are considered ($0°$, $0°$). Using MATLAB, the prepared code completes the collection of 5000 measurements (one set of measurements) in around 30 minutes. These values are stored for further processing using the neural network framework.
Finally, the probe or equipment errors from the dome setup do not contribute much to the losses seen in the dataset but these can be described approximately using a gaussian distribution and are mostly within 5 dB.

3.2. Genetic Algorithm (GA) Overview

Optimization methods are used to find the maximum or minimum of a given objective function *f* as efficiently as possible, subject to all design constraints being satisfied. Initial methods used in global optimizers were deterministic techniques (divide-and-conquer) which were followed later by the more complex stochastic techniques. These included methods like simulated annealing [36], adaptive lagrange multipliers [37], and bio-inspired techniques [38]. The main focus of this thesis is evolutionary algorithms which are also part of global optimizers. Evolutionary algorithms are inspired by biological phenomena and are based on stochastic and/or deterministic update rules which are used to find an optimum solution for the given problem.

Most good heuristic methods are composed of a clever mixture of these two phases (global and lo-

cal); clearly, any method which does not perform a sufficient number of global phases incurs the risk of being trapped in a local minimum, even if run for a very long time. On the other hand, a method which just relies on global phases might be extremely slow to converge to a global solution, as it does not exploit any characteristic of the problem to be solved, such as the continuity of the objective function.

This thesis focuses on a specific type of evolutionary algorithm, the Genetic Algorithm (GA), which is based on the idea of stochastic global optimization. It is based on the idea of natural selection more specifically, the ”survival of the fittest” theory. This optimization technique also allows to set the level of randomization and control. This algorithm is chosen due to its effectiveness with complex objective functions, which is highly dependent on how well the optimization problem is defined. More specifically, due to the binary nature of the problem (0s indicate failed elements and 1s for working elements) it aligns well with the characteristics of the algorithm. Furthermore, due to the binary nature of the problem where 1s represent working elements and 0s represent faulty elements, this algorithm aligns well with these requirements. The precision of the solution is directly influenced by the quality of the equations used in the fitness function and the process of generation. The formulation of the fitness function is very important as it directly affects the accuracy of the solution (determines how ’fit’ each solution is). A simple flowchart for the process is described in Fig. (3.9). The algorithm begins with a randomly chosen group of candidate solutions (chromosomes) which become the initial population and each of these chromosomes is evaluated by the fitness function.

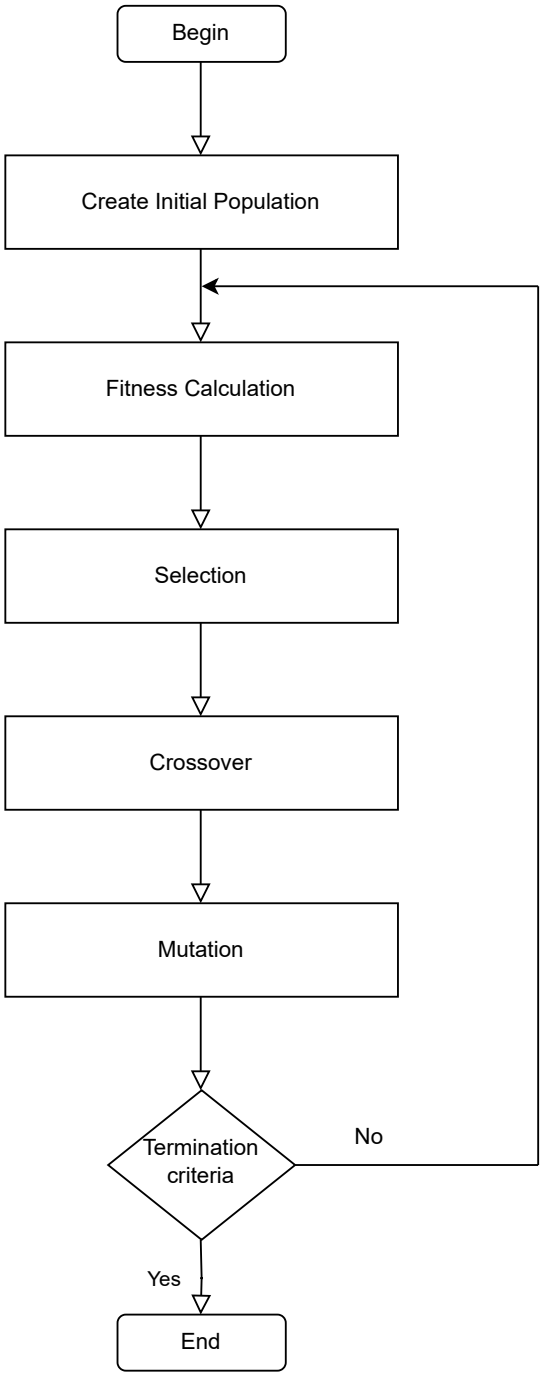

Figure 3.9: Brief outline of the Genetic Algorithm

The three main update rules of GA are selection, mutation and crossover. The selection operator chooses the chromosomes based on how fit the chromosome is (the criterion for which is defined by the user). The crossover operator is inspired by biological crossover and recombining of the chromo-

somes in cell meiosis to create new offspring. Finally, the mutation operator randomly flips individual bits to new chromosomes, to not lose potentially useful genetic material very early in the optimization process. These rules produce the best solutions by working on successive populations iteratively. It starts with generating the initial random population. Then the fitness of each individual is calculated based on a given fitness function. The recognized highly fit individuals process to crossover with other individuals in the population. After the crossover step, the mutation is applied to each child individually, which changes the gene with a small probability. The genetic algorithm has a remarkably high global search ability for exploring and obtaining global solutions. The computational complexity is substantially reduced by using vectorized parameters in this thesis i.e., by reducing the complexity of the problem by reducing the dimensionality which as a result improves the computational time. Through a parallel implementation, time can be further improved, but this is not carried out in this thesis.

3.3. GA Methodology

The methodology used to develop this model and the types of data used in this model are discussed. The rationale behind certain parameters and other choices is justified with a brief overview of the procedure described here. This chapter is structured to first apply the genetic algorithm to array factor data, and then to full wave simulated data. The algorithm has been adapted to suit the problem statement and supports binary output as well.

3.3.1. Initialization

The starting point is an initial population which represents the candidate solutions, only 2 possibilities are considered for the status of each array element (faulty and working represented by 0s and 1s respectively). If partial failures are to be considered, a certain percentage of radiated power decrease, such as 50%, can be assigned to the partially failed element, allowing for modification of the genes (2-bits). However, if multiple percentages of excitation are considered, distinguishing between different cases becomes more complex compared to the former case. So, the chromosome length is set as 64 denoted as *N*, which is the total number of elements in the 8x8 antenna array.

$$C_j = \{a_1, \ldots, a_N\} \tag{3.2}$$

The search is started with a random population of these chromosomes whose fitness is evaluated using an objective function. During successive realizations, the associated fitness of chromosomes in the population is quantified using fitness functions. The population size is also maintained throughout realizations. In this thesis, the population size is 50 for all the simulations. This choice is vital for creating a wide enough search space and increasing the chances of finding the global optimum. The typical population size selected for array diagnosis or synthesis problems is around 100 or lower [39]. To minimize complexity, a population size of 50 was selected as the optimal choice.

3.3.2. Fitness function

The fitness function quantifies the suitability of a solution within a population, it essentially guides the evolutionary process in the GA. Each solution is assigned a fitness value based on how well it meets the objectives of the problem. Depending on the type of problem, these criteria can be designed for minimization or maximization. In this thesis, the fitness function is described in the following equation.

It is essentially the MSE between the observed pattern and the reference pattern. For the first case (array factor, with faults), the MSE is calculated between the faulty and the non-faulty pattern. The second case (full-wave simulations, with faults) is calculated between the patterns with and without mutual coupling. The final case is between the measured data and the reference pattern (with mutual coupling)

$$\rho = \frac{1}{M^2} \sum_{\mathrm{m}=1}^{M} \left(\left| F\hat{F}^m_{obs}(\theta,\phi) \right| - \left| A\hat{F}^m_{ref}(\theta,\phi) \right| \right)^2 \tag{3.3}$$

M is the number of samples used. Based on the minimization of the cost, the position and number of faults can be determined as the outcome. The optimization process continues for the given number of realizations or if a termination criterion is satisfied. In this case, the number of realizations is set as 50.

3.3.3. Selection

In this process, the fittest individuals of the population are selected to create offspring. It also maintains the size of the population throughout multiple realizations and the designed rules for selection help improve the iterative process. Many techniques are present for selection like Roulette Wheel, Cutoff, Tournament and Elitist. In this thesis, the focus is on the Elitist method which favours individuals with the best fitness and who are selected for the next generation. After the fitness is calculated, the first few elite members are chosen after sorting them based on the best fitness values. A modified form of elitism is done so that only a few 'best' chromosomes are copied to be part of the new population.

3.3.4. Crossover and Mutation

The crossover process is to partially exchange genetic information between the parent chromosomes. The single-point crossover technique is used in this research with some conditions based on the crossover probability (Fig. (3.10)).

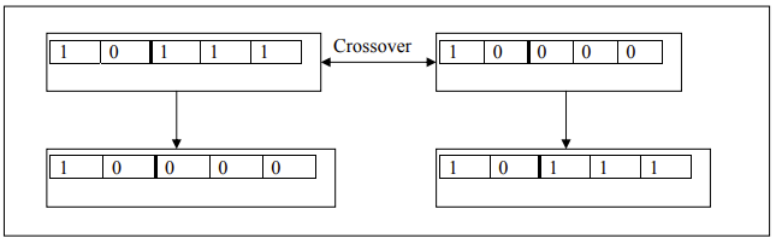

Figure 3.10: Single Point Crossover [40]

Mutation is used to maintain the diversity of the individuals from one population to the next, to prevent them from being trapped in a local optimum [41]. They bring forth the innovation element in the population. Relying on the probability of mutation, elements within the chromosomes are modified. This method uses a simple XOR function to conduct the mutation (flipping as binary values are used). Large mutation rates increase the chances of ruining good chromosomes and might converge quickly hence generally lower mutation rates are used for creating the new population. Therefore, a cross over probability of 0.45 and a mutation probability of 0.1 is chosen.
An important constraint considered while generating new offsprings were to maintain the number of zeroes to be less than the number of faults. As the number of faults for the benchmark topology

has been set as 8 in this thesis, the values must be corrected based on this constraint for each new generation.
The algorithm followed in this optimization method is summarized below,

Algorithm 1 Genetic Algorithm

```
Set initial parameters like nFaults, maxIter, nPop, and so on.
for i = 1 to n_rz do
    Generate random initial population and calculate fitness.
    for iter = 1 to maxIter do
        Perform selection process
        Apply single point crossover on selected parents.
        Apply mutation.
        Calculate fitness scores of the new population.
    end for
    Save best value from each realization.
end for
```

3.4. Conclusions

This heuristic approach is chosen for the binary nature of the problem and is relatively robust to complex data with noisy information. The decisions taken for selecting the probabilities and fitness functions are described in detail in this chapter. For the three different types of data (array factor, full-wave simulated and measured), different parameters are chosen. A basic tuning of the parameters is carried out to decide on the crossover and mutation probability. The size of the search space is vital in determining the time taken for the simulation as well as the convergence to the optimal solution. The performance of this bio-inspired technique is discussed in detail in the Results chapter (5). The computational time, accuracy and overall feasibility is discussed.

4

Machine Learning Model

Machine learning has become one of the most prominent scientific fields in recent years, with numerous applications across various disciplines. Its definition and role can vary significantly depending on the specific area of focus. Machine learning makes predictions or decisions based on data or other informed methods (equations and so on). The human engineering component of this field is vital for the formulation of the problem, organizing data, applying algorithms and validating the results that are obtained. Based on the type of problem, there are different types of machine learning techniques which can be used. Some commonly used ones are artificial neural networks (ANNs), support vector machine (SVM), logistic regression, K-means clustering, and many more. Deep learning is a field of machine learning which mirrors the structure and function of the human brain. Like, the connections between the central nervous system through neurons. They work in layers and typically have more than 3 layers to become deep networks. Therefore, the idea is that deep learning realizes the training of large-scale datasets through the use of a multilevel network and adopts a layer-by-layer extraction method. Firstly, certain steps need to be followed while implementing any ML (machine learning) algorithm to carry out the model and analyses in a systematic manner [42]. A simple workflow has been summarized in the below Fig. (4.1).

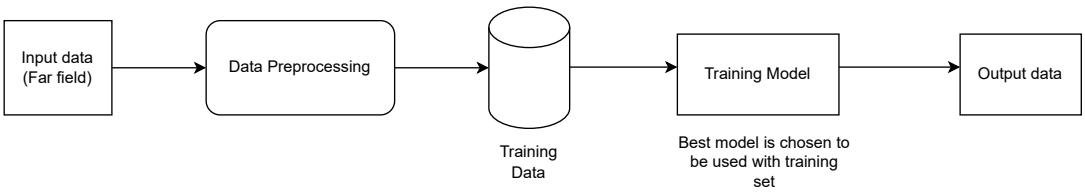

Figure 4.1: Workflow/Pipeline

The different parts of the workflow are explained in detail in the following subsections.

4.1. Input-Output Framework

The first step is to formulate the problem and understand the input and output requirements thoroughly. By understanding this well, it allows for a better choice of ML algorithms and models best suited for the problem at hand. This step justifies the decisions that will be taken later on in the upcoming stages. Fig. (4.2) describes this input-output relation clearly.

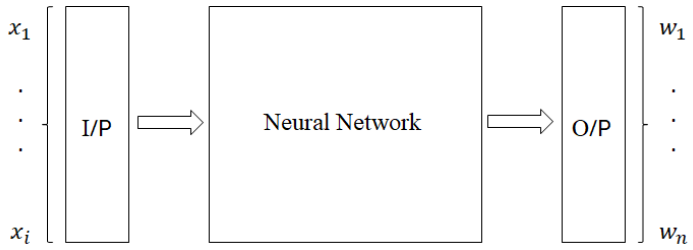

Figure 4.2: Input and Output description

The input is described as $(x_1, x_2, ..., x_i)$ where, i is equal to 36. Essentially, the dome sampling points are considered instead of the entire pattern. The output is described as $(w_1, w_2, ..., w_i)$ where, n is equal to 64 and the values consist of 0s and 1s (binary).
Machine learning has grown into many specialized fields to cater different types of data like text, images, categorical and so on. In this thesis, complex data is generated and the output consists of binary data.

4.2. Type of Model

A small introduction to the types of predictive models present is good for understanding the motivation behind each solution.

Table 4.1: Comparison of different models and amounts of data

	Higher amount of data	**Lower amount of data**
Physics based models	Hybrid models with better prediction	Data driven models to mimic equation based models
Lack of physics based solutions	Data driven models are most preferred	More data is needed to better infer using the model

In this thesis, the starting point is by using some mixed hybrid version of incorporating some physics into the loss function and then finally the purely data-driven models are motivated as they are most suitable for complex measurements.
As the measurements collected cannot be mathematically defined in a closed form equation as they include multiple non-linear effects and setup errors. Due to the black box type nature of the problem formulation in data driven models, this can also prove to be quit challenging. So, this flow will help in motivating the important reference point of using data driven models to make predictions with real time circumstances.

4.3. Data Preprocessing

Data preprocessing is crucial before building an efficient machine learning model. This step involves modifying the generated data to a format suitable for the model. It often includes transformations,

cleaning, and removing missing values or errors. Addressing these issues is essential because they can significantly impact the reliability and accuracy of the ML algorithms' results [43]. Proper preprocessing ensures the data is clean and correctly formatted, leading to more trustworthy and effective model performance. The data generated in this thesis is divided into simulated data and measurement data. So, the results from these studies will also be compared against each other. Measurement data is acquired from the Antenna Dome measurement setup (refer 1.3.1), further regarding this process will be explained in detail in this chapter. The simulated data is far-field data values from Array factor and CST-generated data.
A feature scaling/standardization step is carried out as part of the data preprocessing step in machine learning. This involves the transformation of the dataset into a set of values with a common scale or range (known numerical features). Generated data may not initially be in the same scale or range, which can negatively influence the machine learning model and lead to inaccurate optimization such as dominant biases or misinterpretation of existing features. Normalization/standardization makes sure the features are not affected by the variable ranges and allows for more stable model training. In this thesis, a simple min-max scaling normalization is used to scale the data. The minimum and maximum values from the dataset are used to scale it properly for the **training set**.

$$x' = \frac{x - x_{min}}{x_{max} - x_{min}} \tag{4.1}$$

4.4. Train-Validation Split

Now, that the updated dataset has been created the next step is to carry out the training and validation split. The dataset is divided into two subsets namely, the training set which uses the model to develop relationships within the data. The second subset is the validation set which evaluates the performance of the model and helps understand its shortcomings as well. The third part of the evaluation of the model is using the test set which is used to evaluate the performance of the model to unseen data and are processed separately from the training set to avoid data leakage.

A shuffle is not required during the training and validation split as the data in the training set are already from randomly generated faulty elements so it does not require further shuffling. The training and validation split carried out in this thesis is 80% and 20%. It provides a good balance between the training and validation data. Initially, a 90-10% split was considered but sufficient validation data is also required to capture the underlying patterns. The (80-20) split also provides computational efficiency without excess resource usage.

4.5. Computational Framework

The programming platform used to design the NNs and carry out the simulations is PyCharm 2023.3.3. Python is the programming language, as it is very well known for existing Machine learning modules for multiple problem statements. Based on the input and output types, there is lot of community support regarding each type of formulation. The machine learning platform used is TensorFlow, it is an open source deep learning library developed but the Google Brain team. The library uses high level APIs like Keras for running complex simulations and optimizing the models. Also has added functionality like tensor board for visualizing the convergence of loss plots and comprehensive understanding of the deep learning environment.

4.6. Fully Connected Network Model

The most common ANN architecture is the FCNN (Fully Connected NN). This type of NN is where all the neurons are connected to their previous and following layers. The weights indicate the importance of the neurons which is quantified by the activation function. The model developed has 10 layers of increasing density up to a few layers, and the layer sizes are adjusted according to the output requirements. The first layer is the input layer, which receives the data; the last layer delivers the classification result. The layers in the middle are the hidden layers which operate and explain the behaviour of each neuron. The non-linearization of the data is carried out through the help of activation functions. A probability threshold (p) is set to define to which of the two classes the data, in a binary problem, the data belongs. If the output number is larger than the threshold (0.5), the given class is assigned. If a high threshold is chosen indicating a high level of confidence the model is more rigorous and makes fewer positive detections. But for a low threshold, false detections will increase. So choosing the threshold is quite important for making the predictions. The batch normalization layers are implemented for normalizing the input to the respective layer, to maintain stability concerning the current batch and improves the training speed. Some drop layers are included as well to prevent the over fitting of data by randomly dropping neurons during the training at a mentioned rate. The size of the network was maintained as small as possible to obtain the desired results. The NN architecture is described below in Fig.(4.3),

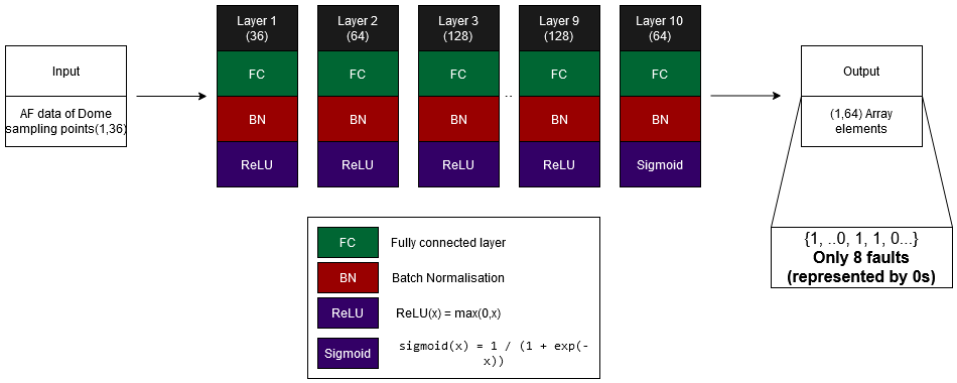

Figure 4.3: Proposed Architecture

So, the fully connected network provides the 8 faulty elements and their position in the binary form where 0s represent faulty elements and 1s are the working elements. The initial layers have ReLU activation and the final layer uses Sigmoid activation as the desired output is binary form.
For the 2 and 4 fault scenarios, the architecture used for the fully connected network remains the same, except for the addition of a few more hidden dense layers. But the main difference is an additional sparse convolutional layer is added in the beginning which is then flattened and used as normal input to the fully connected network.

4.6.1. Activation and loss functions

The activation functions used in this model are ReLU and Sigmoid. For the measurement data, a similar activation function called GeLU is used to create smoother plots and obtain better convergence.
The ReLU function introduces non-linearities in the layers of the model, this lets the network learn complex relationships in the dataset. It is simple and is more efficient in comparison to other complex parabolic function like tanh. Also, allows for sparse activation which increases the efficiency of finding

the patterns in the data.

$$\text{ReLU}(x) = \max(0, x) \tag{4.2}$$

The Sigmoid activation function is used in the final layer as it exists between the range 0 and 1 and provides the probabilities for the same which can be used to make predictions by selecting a threshold. The function is also differentiable and is widely used in binary classification problems.

$$\sigma(x) = \frac{1}{1 + e^{-x}} \tag{4.3}$$

For the data from the measurements, the GeLU (Gaussian Error Linear Units) activation is used as it proves to have a smoother convergence in comparison to the ReLU and can capture more complex relationships.

$$\text{GeLU}(x) = 0.5x \left(1 + \tanh\left[\sqrt{\frac{2}{\pi}}\left(x + 0.044715x^3\right)\right]\right) \tag{4.4}$$

The difference between these functions can be illustrated using Fig.(4.4) shown below.

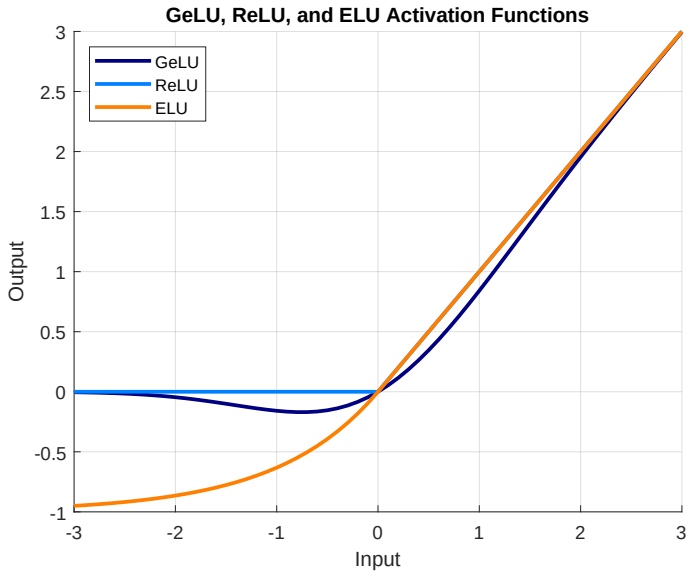

Figure 4.4: GeLU, ReLU and ELU

The optimizer of choice for this model is ADAM (Adaptive moment estimation) is an adaptive learning rate optimization algorithm which is designed for deep neural networks [44]. It is a combination of RMSProp (gradient based optimization, learning rate is a hyper parameter) and Momentum. This optimizer calculates the learning rates for every parameter and preserves that epochs squared gradients with the average gradients [45]. It is often preferred as it has low computational costs and is known to robustly adapt to large datasets and deep neural networks. The adjusted parameters are defined for time $(t+1)$ as follows,

$$\begin{aligned} \mathsf{m_t} &= \beta_1 \cdot \mathsf{m_{t-1}} + (1-\beta_1) \cdot \mathsf{g}_t \\ \widehat{m}_\mathsf{t} &= \mathsf{m_t} / \left(1-\beta_1^t\right) \\ \mathsf{v_t} &= \beta_2 \cdot \mathsf{v_{t-1}} + (1-\beta_2) \cdot \mathsf{g}_t \\ \hat{\mathsf{v}}_\mathsf{t} &= \mathsf{v_t} / \left(1-\beta_2^t\right) \\ \theta_{\mathsf{t}+1} &= \theta_\mathsf{t} - \frac{\eta}{\sqrt{v_{\mathsf{tt}}+\varepsilon}} \cdot \hat{\mathsf{m}}_\mathsf{t} \end{aligned} \tag{4.5}$$

where $\hat{\mathsf{v}}_\mathsf{t}$ is the bias corrected value in the previous epoch and $\mathsf{m_t}$ is the bias corrected value for the previous average gradient. Moving onto the modified loss function which is used in the case of simulated and measurement data,
Binary cross entropy loss is used for classification tasks with mostly a positive and negative label. It measures the differences between the predicted probabilities and true binary labels. So the model itself encourages higher probabilities for working and lower for faulty. It is represented in the following equation,

$$bce = -\frac{1}{n}\sum_{i=1}^{n}\left[y_{\mathsf{true}}^{(i)}\ \mathsf{log}\left(y_{\mathsf{pred}}^{(i)}\right) + \left(1-y_{\mathsf{true}}^{(i)}\right)\mathsf{log}\left(1-y_{\mathsf{pred}}^{(i)}\right)\right] \tag{4.6}$$

It works very well with the sigmoid function which is used in the output layer of this model. Now, a custom penalty function is created which penalizes the network when it detects higher than 8 number of faults. So, the number is restricted and the network knows only to look for 8 faulty elements. Furthermore, a small error value is also added to include the position error with respect to the target values.

$$p = bce + 10 * (|y_{\mathsf{pred}}| - 56) + e \tag{4.7}$$

Success ratio metric is defined using the equation below [46],

$$\begin{aligned} \mathsf{numel}(i) &= \mathsf{numel}\left(\{D_d(i) \cap D\}\right). \\ \eta &= \frac{\sum_{i=1}^{nM} \mathsf{numel}(i)}{(n)} * 100\% \end{aligned} \tag{4.8}$$

Here, i runs through the number of measurements. numel(i) is the number of failures correctly diagnosed on the i^{th} test and, n is the number of faulty elements considered. Finally, D_d are the diagnosed elements and D are the target elements.
Furthermore, numel in terms of MATLAB can be defined as the function which returns the number of elements in a given array, usually equivalent to the product of the array dimensions.

In addition to this model, a few additions have been made to accommodate for the different number of faults. These results from varying faults are discussed in detail in the Results chapter (5).

4.6.2. Evaluating the Model

During an epoch, the loss function is calculated across all the data points and gives the loss measure at the given epoch. But plotting the curve across iterations gives the loss of the particular subset instead of the entire dataset so this is more suitable for the problem at hand.
Learning curves are a very common visualization and diagnostic tool in machine learning algorithms. These curves display the evaluated results of the training and validation set after every consecutive

update; the performance is plotted to conduct further analyses. Fig. (4.5) is used to describe such curves.

The training set learning curve shows the ability of the network to learn and the validation learning curve quantifies the ability of the network to generalize based on a hold-out validation dataset. A short explanation of the three commonly seen observations on learning curves is under-fitting, overfitting and good fit. A good fit is self-explanatory, where both loss and accuracy are obtained as expected. Underfitting is when the model is not able to reach low error values using the training set. Overfitting is when the model has learnt the training set too well and is not able to generalize for new datasets.

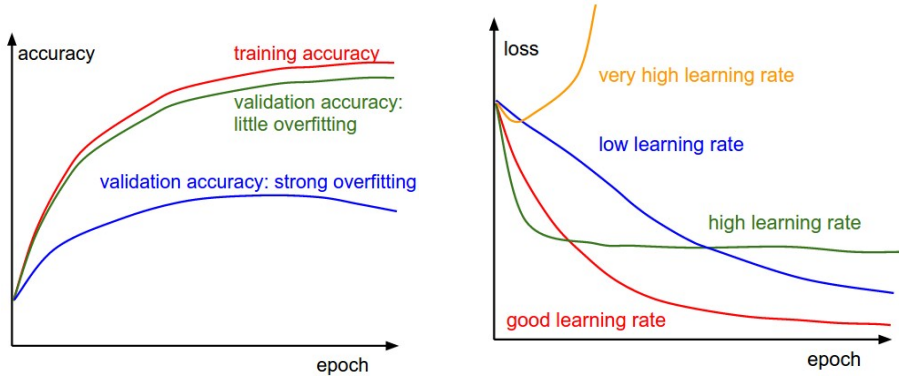

(a) Accuracy plot **(b)** Loss plot

Figure 4.5: Accuracy and Loss Description plots ([47])

Evaluation of the Effects of Different Dataset sizes

The measurement dataset has 5000 samples in total. This is divided into 1000-3000-5000 sized datasets to discern the amount of data required by the network to arrive at the desired result. For using 5000 measurements (entire sample set), the results obtained from the network are shown in Fig. (4.6),

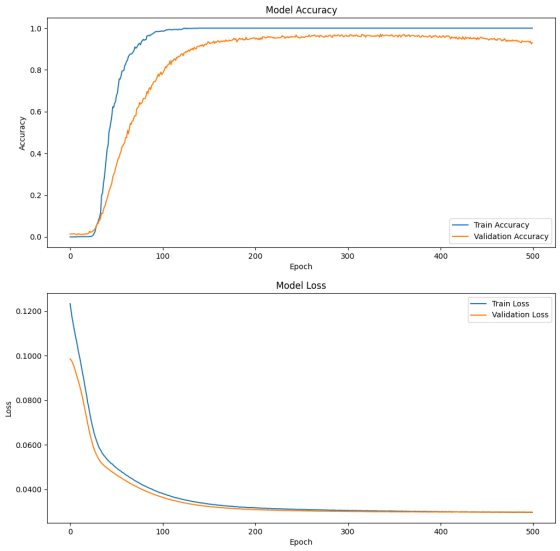

Figure 4.6: Accuracy and Loss plots (5000 measurements, 8 failures)

The validation accuracy obtained is 95.25% which demonstrates a good learning rate and little overfitting. The lowest loss value is 0.027. The failure rate that is considered is 12.5% and this remains constant throughout this thesis, but the success ratio depends on not just the failure rate but also the dataset size and variation in power levels. The accuracy of the 3000 measurement set is 92% and the minimum loss value is 0.02 as shown in Fig. (4.7).

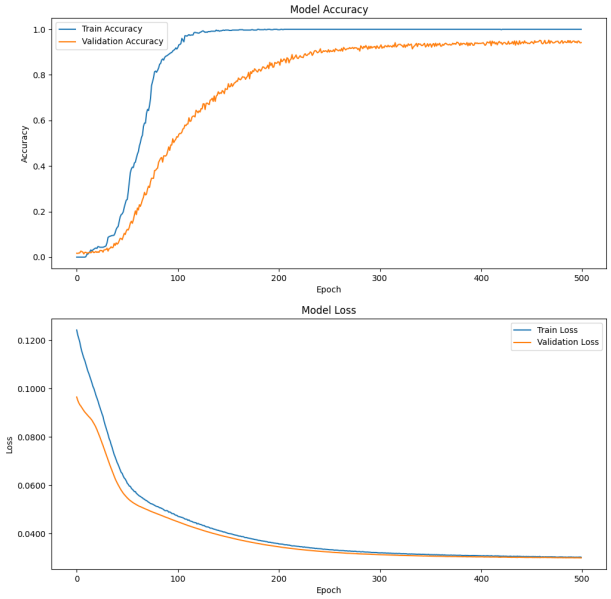

Figure 4.7: Accuracy and Loss plots (3000 measurements, 8 failures)

For 1000 measurements, the accuracy is reduced to 89% and has a loss value of 0.032. With the decrease in the size of the dataset, it can be seen in Fig. (4.8) that the convergence is much slower (as a higher number of epochs are utilised for smaller datasets) and is not as smooth with a larger amount of data. One point to note would be that the values do not reach zero, as this data is highly non-linear so it is not possible to obtain the same results as with the ideal data. But in that case, based on the failure rate the diagnosis success rate keeps improving. Even in the case of 1000 measurements, a redefined network with reduced complexity and more regularization.

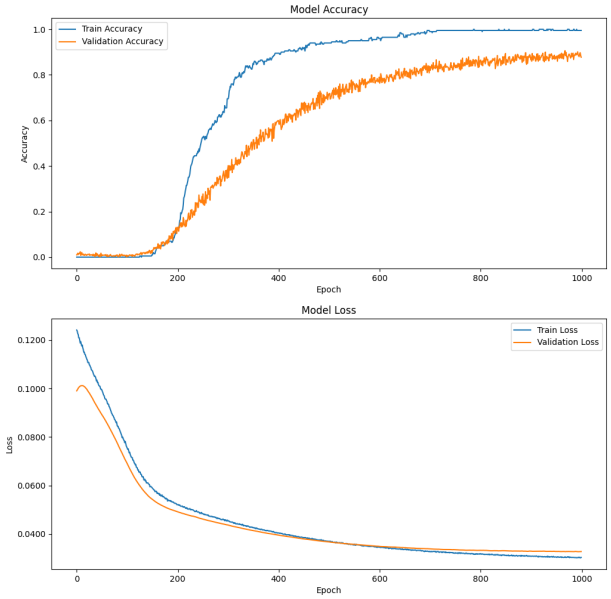

Figure 4.8: Accuracy and Loss plots (1000 measurements, 8 failures)

As in the case of 1000 measurements, the results start to reach the optimum convergence only after 400 epochs whereas, for the other two measurement sizes, there is very little overfitting and quickly converges to the optimum loss value. In general, the collection of more data and simulating more epochs (like 5000 or higher) would lead to better convergence rates. The success ratio depreciates from the 5000 measurement dataset to the lowest (1000 measurements)).

4.7. Conclusions

This chapter mainly discusses some machine learning basics and the framework used in this thesis. The models which include the physics behind the problem are used for the array factor data and slowly transition to the data-driven models. As the array factor and full-wave simulated data can be described closely using equations, they are used first with the model, and then to a purely data-driven model where the losses are defined according to the required predicted result. Some data preprocessing is also carried out to provide cleaner data to be processed by the model effectively. Two specific activation functions that are explored in this thesis, the GeLU and ReLU activation. Followed by a modified loss function for specific number of fault scenarios. In the Results chapter (5) detailed discussions are done for varying number of faults and sampling points.

5

Results and Discussion

In this chapter, some statistical studies are carried out to compare different topologies with the GA and ML algorithms. The performance of both the GA and ML are compared with the number of correct predictions for different types of data. The three types of data considered here are namely,

- Array factor data;
- Full-wave simulated data;
- Measured data.

In some cases of 2 and 4 faults, the comparison between full-wave simulated and measured data is conducted for both algorithms.

5.1. 8-Element Failures

5.1.1. GA Results

The optimizer is applied under different conditions for three types of data as mentioned in section (3.3.2).

- Case 1: Fault and non-faulty pattern (array factor)
- Case 2: With MC and without MC (full-wave simulated, with faults)
- Case 3: Measured pattern and full-wave simulated (with faults)

The parameters for the optimizer are tuned to find the best probabilities in each scenario. Some of these studies will be discussed in this section.

Array Factor Data

The GA parameters used in this optimization are presented in Table (5.1).
The time taken for the simulation is around 16 hours using a standard desktop computer. The results from each realization are stored as well as the best cost values from each generation. Figure (5.1a) illustrates the region of convergence and the optimum solution achieved by the GA.

Table 5.1: Optimization Parameters - Case 1

Parameters	Values
Number of faults	8
Number of realizations	50
Number of Iterations	1000
Crossover probability	0.45
Mutation Probability	0.1
Population Size	50

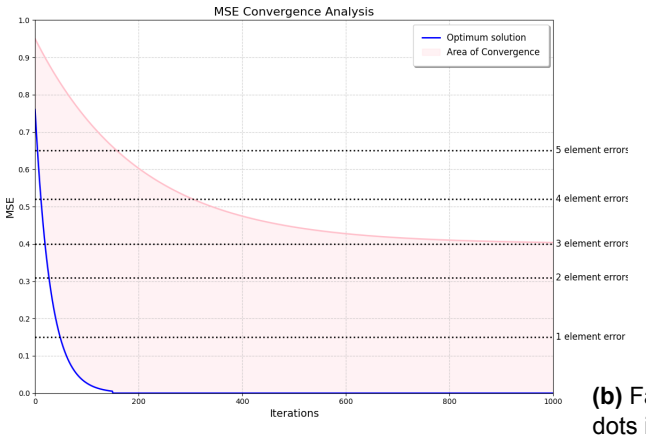

(a) MSE v Iterations plot

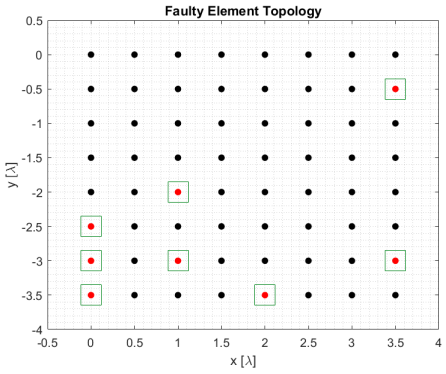

(b) Faulty element topology with predictions where red dots indicate the faulty elements, green boxes indicate the predictions

Figure 5.1: Case 1: Array factor data with 8-element failures.

In Fig. (5.3b), the predicted values are highlighted using green boxes and faulty elements using red dots. For this considered topology, the GA was able to correctly predict all the faulty elements. In Fig. (5.1a), the blue line in the plot represents the optimum solution, showing proper convergence to the optimum solution. This indicates that the optimizer successfully reached the results in approximately 200 iterations. The area of convergence is the region which indicates the variation of MSE values with varying realizations and increasing iterations. To be more specific, there are multiple results which converge to zero but not always at the same iteration as the optimizer runs for 50 realizations as well. The plot also indicates the number of errors in the predicted values corresponding to the respective MSE value. To be more clear, the element error essentially implies that the optimizer incorrectly predicted one or more elements compared to the true solution. It indicates the effectiveness of the algorithm for fault detection with a certain number of faults. The algorithm slowly refines the solutions over the iterations and converges at the optimum solution. A significant issue with this approach is that it necessitates a large number of simulations and computations to achieve reliable results. Even though the generation of data is not costly but based on the number of realizations and iterations the process becomes more expensive.

Further studies are conducted based on varying number of faults to understand their effects on the performance of the GA. The studies on their position are already completed in the deterministic study in Chapter 2. Now, the best cost values are collected through an increasing number of realizations (studied till the earliest so, from 0 to 25) for varying number of faults.

Initially, a description of the general trend would be of good use. Fig. (5.2) shows a decreasing trend in the cost function values as the number of realizations increases, indicating that the optimization process is effective in improving the solution quality over time. These lines are plotted with an increasing number

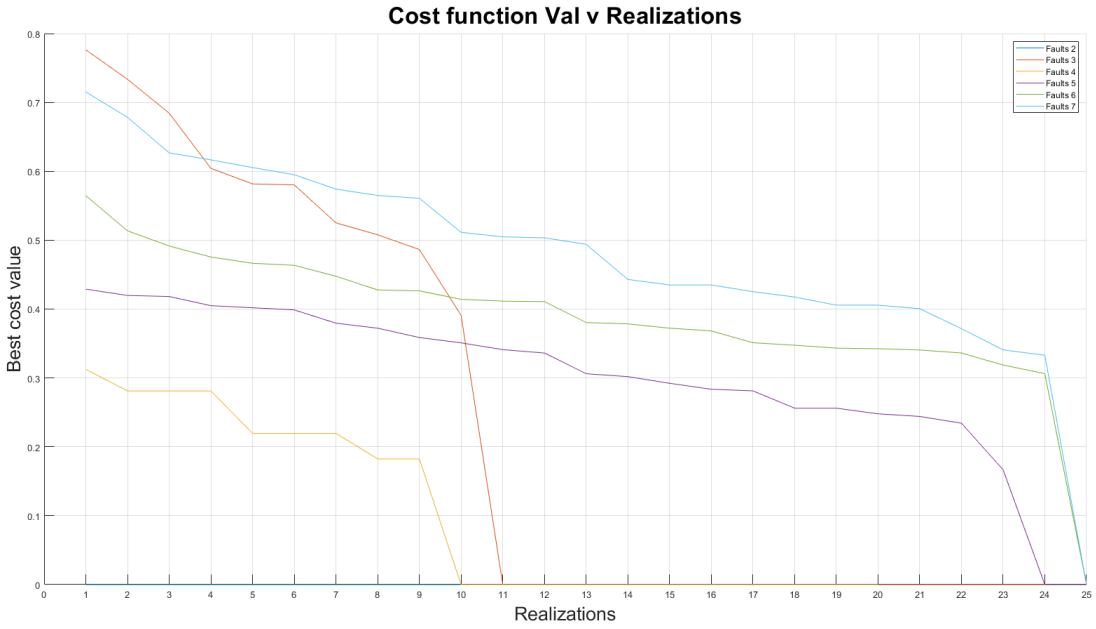

Figure 5.2: Analysis of the GA for the varying number faulty elements.

of faults and the simulations are run for 30 realizations, but the plot is to indicate in which realization the value reaches the optimum solution. For smaller number of faults, the convergence of the cost value to 0 occurs much more quickly in comparison to higher numbers like 6 or 7. Also for different numbers of faults, the slopes are highly varying as well. the rate of convergence is smoother as the number of faults increases in comparison to a smaller number of faults. As seen for the three faults case, the cost is quite high and drops quickly like a discrete step. Finally, the plot also demonstrates that all fault scenarios eventually stabilize, reaching a point where additional realizations bring minimal further improvement. This stabilization suggests that the algorithm has effectively minimized the cost function for each fault scenario.
All of these observations help in understanding the limitations of the algorithm and how effective it is for different scenarios. For a smaller number of faults, this algorithm is fast and effective in ideal conditions.

Full-wave Simulated Data

As mentioned in the data generation section (3.1.1), the full-wave simulated data is obtained from CST and the array pattern is calculated using that. The patterns include faults to make an accurate comparison. The parameters used in this scenario are described in Table (5.5).

Table 5.2: Optimization Parameters - CST data

Parameters	**Values**
Number of faults	8
Number of realizations	50
Number of Iterations	2000
Crossover probability	0.45
Mutation Probability	0.05
Population Size	50

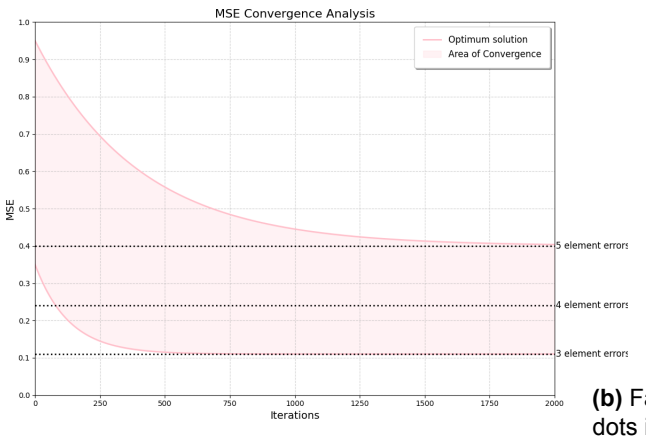

(a) MSE v Iterations - Including MC

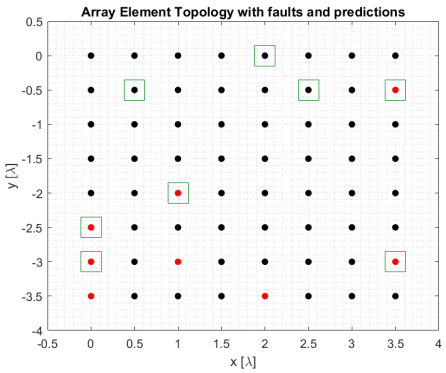

(b) Faulty element topology with predictions where red dots indicate the faulty elements, green boxes indicate the predictions

Figure 5.3: Case 2: Full-wave simulated data with 8-element failures

A chosen topology is described in Fig. (5.3) along with the predictions and GA convergence plot, similar to the discussion using the Array factor data. Now, visualizing the pattern in Fig. (5.4) the target and predicted topologies are compared. The overall pattern seems similar but there is some pattern distortion that can be seen mainly in the sidelobes. The power distribution for the sidelobes is also varying in the predicted pattern. The time taken for this algorithm is comparable to other studies using the genetic algorithm. However, it is still too computationally intensive and is not a feasible solution for real-time/ fast determination of faulty elements in 2D antenna arrays.

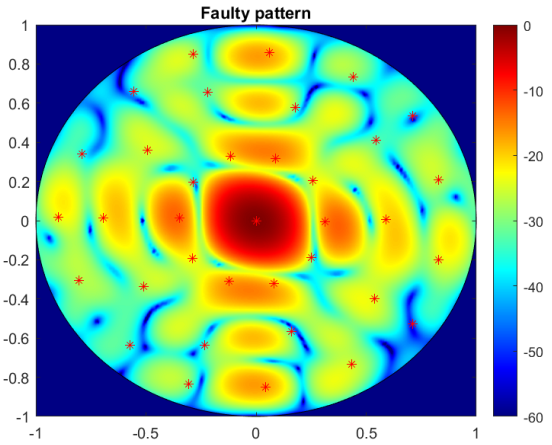

(a) UV plot with chosen faulty topology

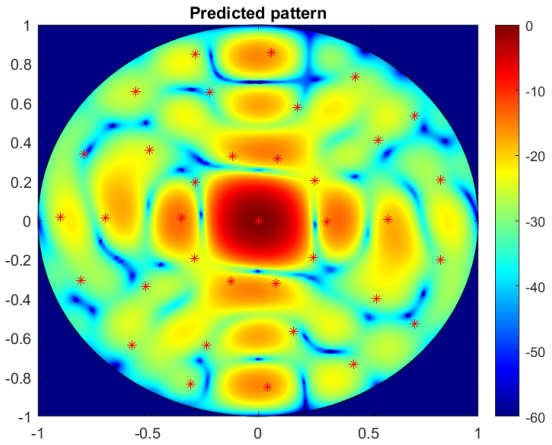

(b) UV plot of predicted faults using GA

Figure 5.4: UV plots of faulty and predicted patterns with 8 faulty elements (GA)

Measured Data

The final case is when the measured data are used for the GA. The faulty element topology and the predicted elements are highlighted in Fig. (5.5). Here, the comparison between the faulty and predicted measured values are shown in Fig. (5.6).

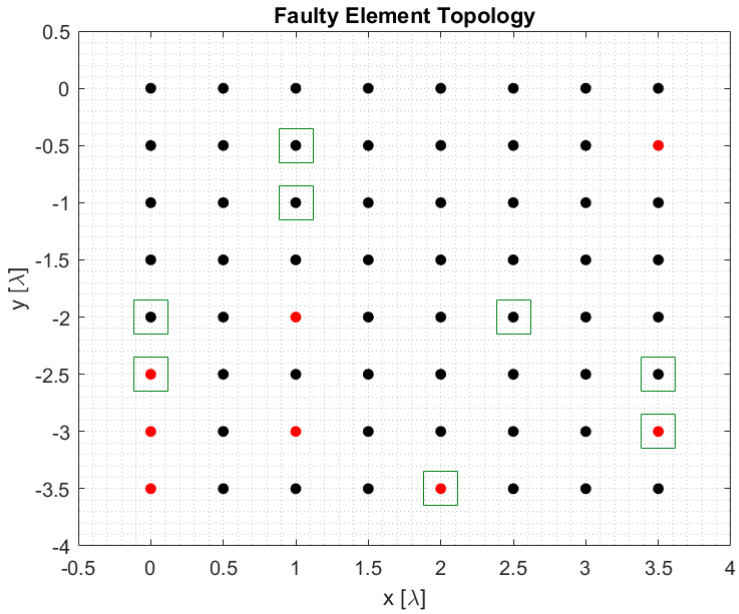

Figure 5.5: Array element topology with 8 faulty elements and the predictions. Red dots indicate the faulty elements, green boxes indicate the predictions.

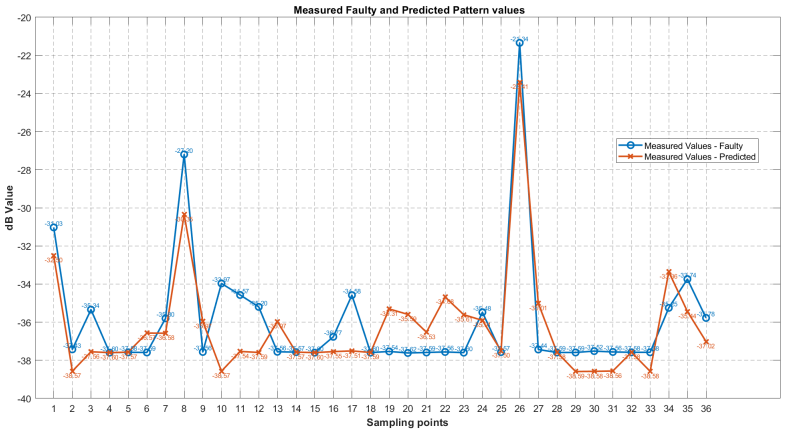

Figure 5.6: Measured pattern compared with predicted and input for 8 faulty elements.

From this one such topology, the GA can predict three elements correctly. Although the major trend is followed by the predicted value, it is still varying from the target pattern. In the topology, it can also be seen that the predicted elements are not near the region of the faults either. As the GA takes on a randomized approach to explore, it is not always able to achieve a region-wise diagnosis.
In Fig.(5.7), statistics of 100 random topologies are displayed. The number of correct predictions against the topology is studied. A more comprehensive analysis is conducted in the following chapter whilst comparing it with the machine-learning method.

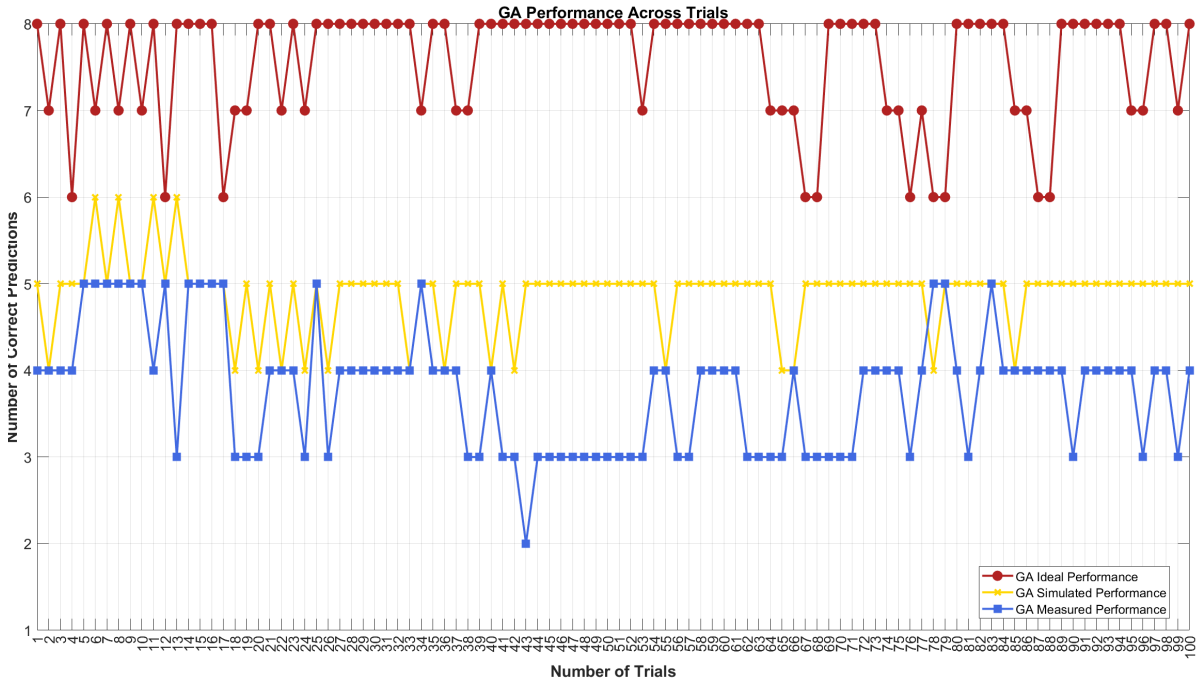

Figure 5.7: GA predictions for array factor, full-wave simulated and measured data for the 8-element failure case.

As expected, it can be seen that the GA performs well with the array factor data and simulated data. However, it is not able to achieve desirable results with the measured data. For simulated data mostly 5 elements are predicted correctly and the results of one such topology are discussed in detail in Section (5.1.1). For measured data, mostly correct predictions lie with 3-4 elements with the lowest correct predictions being two.

5.1.2. ML Results

The aim is to make sure the network can accommodate the demands of the phased array with and without mutual coupling. Initially, the network is provided with the Array factor equation in the loss function so that it can be used to discern the stability of the network and ensure convergence to the optimal solution. The parameter values are, a learning rate of 0.001, batch size of 32, and dropout layers are added to prevent overfitting, with decreasing l2-regularization (especially for the second result). Mostly, the fundamental values of the parameters are used.

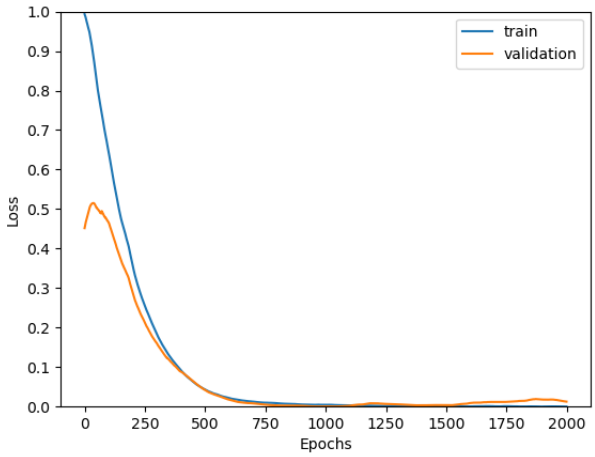

Figure 5.8: Loss plot using Ideal AF data for the 8-element failure case.

Figure (5.8) can be effectively used to compare the performance of the machine learning algorithm to the benchmark result. The decay of the loss function is smooth and achieves the convergence to the optimal solution near 600 epochs. The training data as expected converges more smoothly compared to the validation set. The model can predict the targets as expected. The time taken for this simulation (includes the computation of AF loss function (eq. 3.3) but instead with the true and predicted value) is 4.2 hours. The important thing is this simulation was carried out without any GPU, but if they were used, this time could be improved to 1/10th of the value obtained. It is currently run on a 2.2 GHz Intel Core processor on a PC.

Here, are the results with MC (mutual coupling) effects added to the dataset in Fig. (5.9). The synthetic noise as mentioned before in Section (3.1.1) is generated to be as close as possible to the measured data. Furthermore, all the results from now on are purely data-driven models where description of the loss function is given in detail in Section (4.6.1).

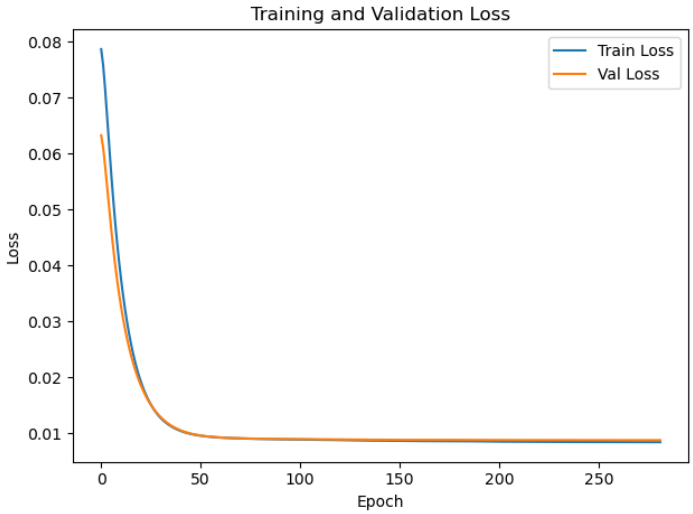

Figure 5.9: Loss plot for full-wave simulated data for 8-element failure case.

The lowest loss value is 0.01 and the convergence occurs around 100 epochs. An early stopping

criteria is also specified for validation loss. Using generated data with the custom loss function, the predicted values have 80% success ratio with 1-2 element fails. But the overall pattern is preserved with minimal changes in the far sidelobes. The general time taken for the purely data-driven models is around or within 30 minutes.
A comprehensive comparison of over 100 trials for multiple cases is conducted in Section (5.13). For the ML predictions, the number of correct predictions is mostly around 7 out of 8 for the simulated data. The resultant single-element error is also present close to the region of the target fault. This can be seen through an example topology in Fig. (5.10).

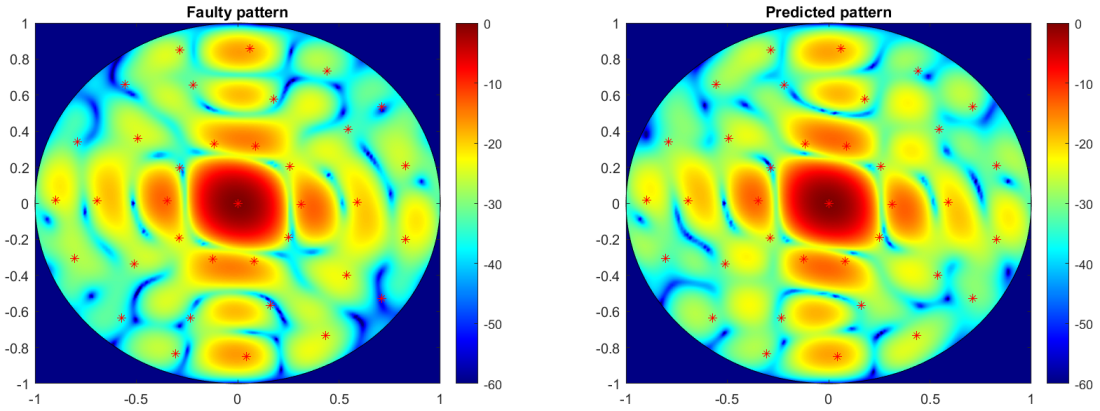

(a) UV plot using faulty topology

(b) UV plot of predicted topology.

Figure 5.10: UV plots for full-wave simulated data for 8-element failures with red stars indicating the DOME sampling points.

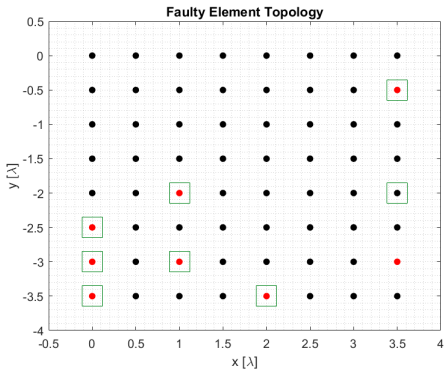

Figure 5.11: Array element topology with faults and predictions for 8-element failure where red dots indicate the faulty elements, green boxes indicate the predictions.

The final case uses measured data and the comparison of predictions with GA and ML is discussed in the below Fig. (5.12). The target pattern compared to the predicted is similar and even with a single element error most of the information from the original pattern is retained. Furthermore, a single-element error case is highlighted to further show that the ML can indicate the region of the faults in all cases and retain the pattern characteristics as well.

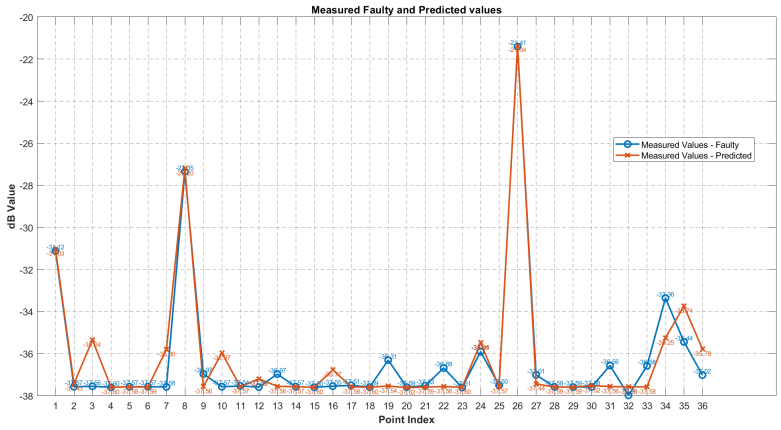

(a) Measured data pattern comparison for 8 faulty elements (7 out of 8 predicted).

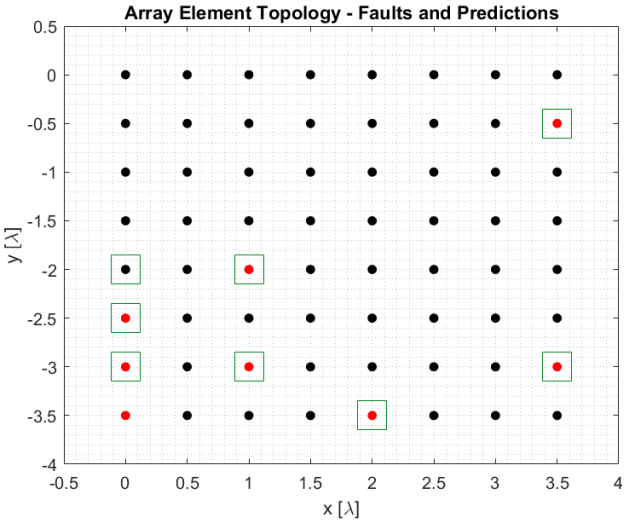

(b) Array element topology with faults and predictions where red dots indicate the faulty elements, green boxes indicate the predictions

Figure 5.12: 7 out of 8 elements correct predictions scenario for the 8-element failure case.

5.1.3. Comparison Plots for 8-Element Failures

Although it takes a few more hours to converge to the optimum solution using the GA, it is an acceptable lead time for rectifying faults in a real setup in remote regions or with difficult terrain. However real-time fast detection is necessary to improve and allow more efficient methods in the antenna recovery process as well. This trade-off takes priority on a case-to-case basis. Major takeaways from the GA are that after including highly non-linear effects to the data used by the optimizer, the simulations are highly computationally intensive and time-consuming with no guarantee of arriving at the global optimum. It is impossible to correctly formulate a closed-form solution that generates accurate candidate solutions for this problem. The array factor-based equations work well with this heuristic approach, but once more non-linearities are included like MC effects and measurement errors, a complete 8 correct predictions were not achieved. Hence, there is a need for machine learning assisted techniques which are also able to work with black box functions and can be guided to work for specific datasets as well.

The statistical studies after comparing both optimizer models are discussed in this chapter. Based on decreased computational time and accuracy, the ML outperforms the GA. Few trials explain how the ML proves region-wise diagnosis possible as well (sub-arrays). Around 60/100 trials give single-element errors and some exactly correct predictions with detailed analyses discussed above. With a larger dataset of 10,000 or higher measurements, this can be improved significantly. The use of large datasets is also considered for varying number of faults. As for a lesser number of faults, there is a need for a higher amount of data to study the patterns. The impact of the faults on the radiation pattern decreases with a lower number of faults.
The results for the comparison across 100 different array topologies are shown in Fig. (5.13).

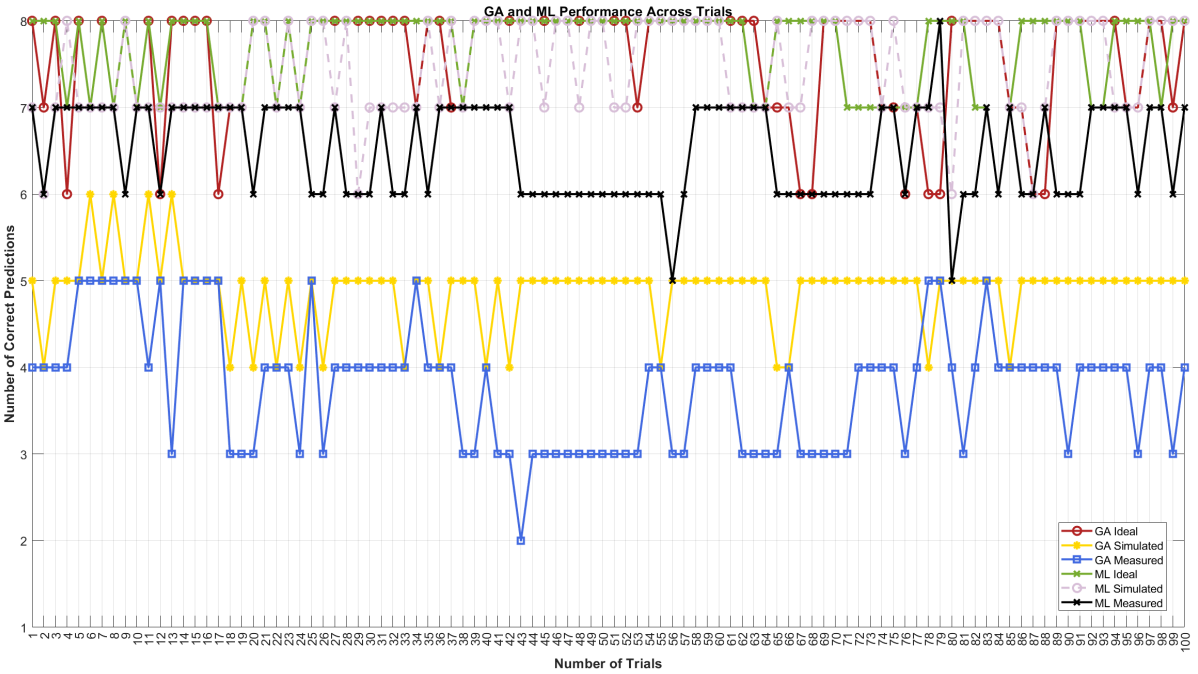

Figure 5.13: Predictions of GA and ML for 100 topologies from the validation set for 8-element failures

In Fig. (5.13), it can be seen that the GA and ML perform quite well with array factor data. Compared to computational time, ML is much faster compared to GA. 76/100 topologies are predicted correctly using ML and 66/100 topologies are predicted exactly with 8 correct predictions using GA. In some topologies, there is a poor performance from both GA and ML, but if an example of these is studied ML can predict the region of the failed element correctly whereas the GA predictions are more random in comparison.

5.2. 4-Element Failures

In this section, a discussion regarding the performance of both optimizers (GA and ML) are conducted. Due to time constraints, the full-wave simulated data and the measured data are compared for 100 trials to derive some statistics from the predicted results and the parameters are chosen accordingly.

5.2.1. GA Results

Full-wave Simulated Data

In this section, one such topology from the validation set is analysed and compared for the measured and simulated. The detailed comparison between 100 different trials is discussed in Section (5.2.3). The parameters used for this simulation are shown in Table (5.3).

Table 5.3: Optimization Parameters - Full-wave simulated data

Parameters	**Values**
Number of faults	4
Number of realizations	25
Number of Iterations	1000
Crossover probability	0.4
Mutation Probability	0.05
Population Size	50

An example from the validation set is chosen to illustrate the problem. The original faulty pattern for 4-element failures of the chosen case is shown in Fig. (5.14).

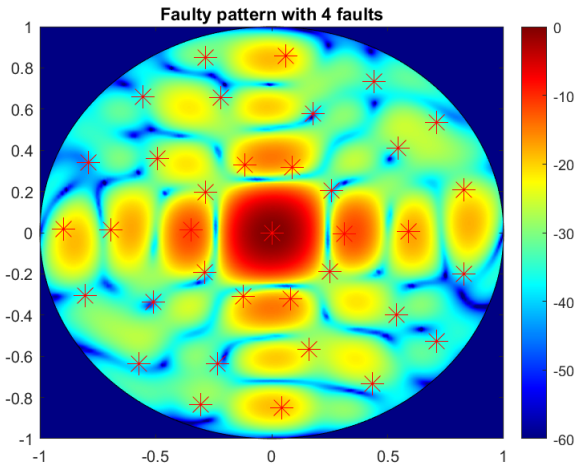

Figure 5.14: UV plot of full-wave simulated pattern with 4-element failures with red stars indicating the DOME sampling points.

The results obtained from GA are shown in Fig.(5.15). It can be seen that there are two errors in prediction results. Partially able to diagnose the region as well. A parallel comparison with the ML predictions is also carried out to check the results (Section (**??**)).

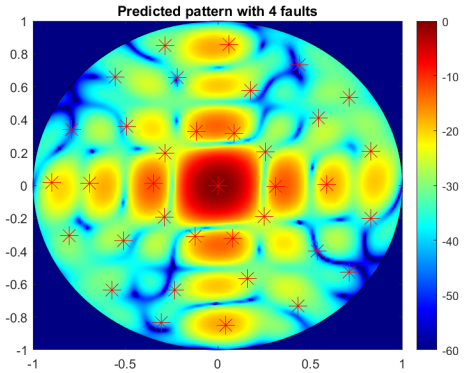

(a) Full-wave simulated pattern with 4-element failures where red dots indicate the faulty elements, green boxes indicate the predictions

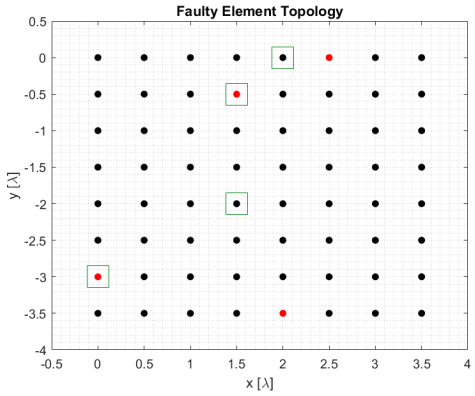

(b) Array element topology with predictions where red dots indicate the faulty elements, green boxes indicate the predictions

Figure 5.15: GA method predicted pattern and topology for 4-element failures.

Measured Data

For the same topology, the results from the measurements are considered and compared with the predicted and the original element topology.

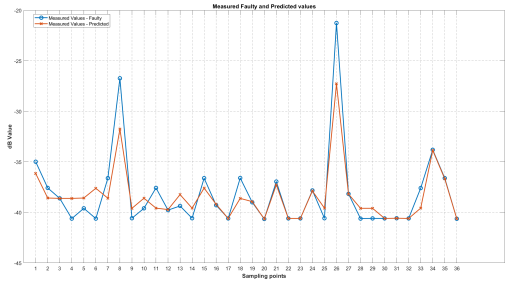

(a) Measured result comparison with 4 faults

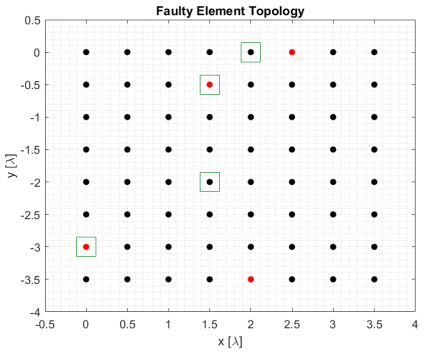

(b) Array element topology with predictions (4 faults)

Figure 5.16: GA method predicted pattern and topology for 4 failures.

5.2.2. ML Results

In this section, the results from the ML method are discussed. A specific topology is explored in detail comparing their UV plots and many more, ending with a comparison plot which depicts the overall performance of the method over a fixed number of trials (in this thesis, 100 trials). For the measured data, the amount of data collected from the measurement setup is 10,000 samples. A comprehensive test and comparison between GA and ML for its validation size is beyond the timeline of this thesis. However, the entire validation set is explored for all three types of faults using only the Machine learning method for special cases like using just certain rings in an upcoming section (Section. (5.4)).

Full-wave Simulated Data

In this section, similar to the previous results the same topology is compared. In the previous section, the performance of the GA method is discussed where there are 3 number of correct predictions for full-wave simulated data and for the measured case 2 correct predictions are made. The comparison with these results can lead to some interesting conclusions. Figure (5.17)) illustrates the results from the ML method for the original topology (5.14).

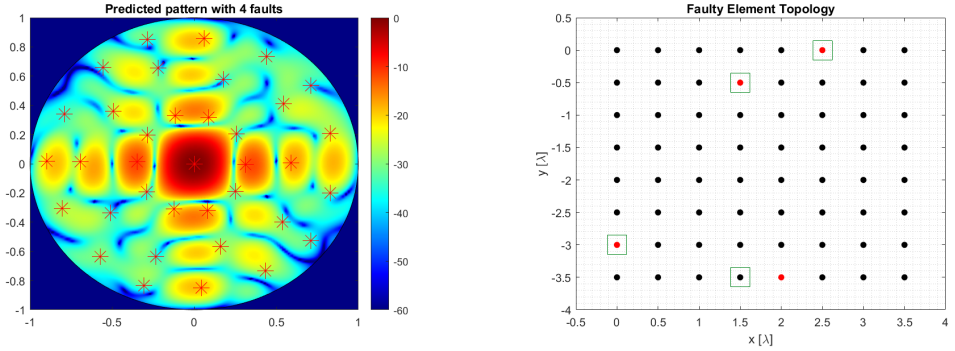

(a) Full-wave simulated pattern with 4-element failures where red stars indicating the DOME sampling points

(b) Array element topology with predictions where red dots indicate the faulty elements, green boxes indicate the predictions

Figure 5.17: ML method simulated data results for 4-element failure case.

Here, it is seen that the single incorrectly predicted element is also diagnosed very close to the region of the target element. There are a few observable changes in the sidelobes but, the overall pattern remains the same.

Measured Data

The results from considering the values from the measurement setup with 4 faulty elements are used to carry out the predictions. Similar to the GA method plots, the predicted and original are compared, and the same procedure is carried out here. Figure (5.18) represents the dB values from the sensor nodes and the corresponding topology.

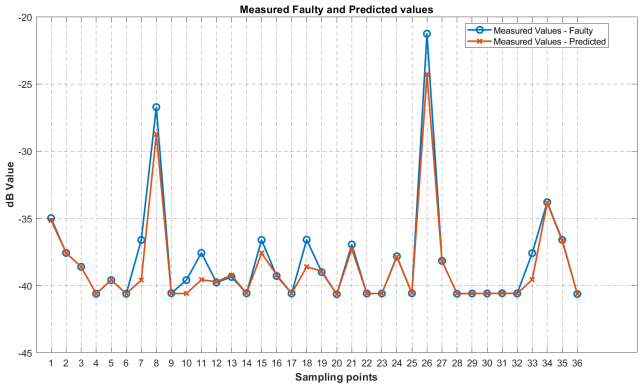

(a) Measured and predicted results comparison for the 4-element failure case

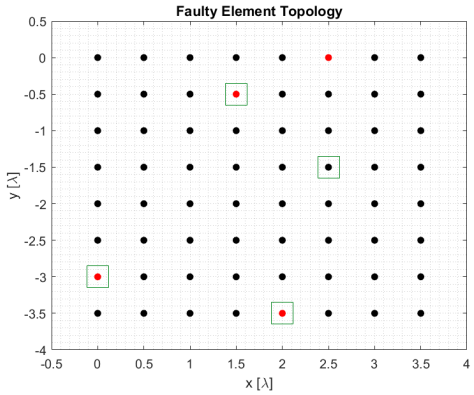

(b) Corresponding case topology with predictions where red dots indicate the faulty elements, green boxes indicate the predictions

Figure 5.18: ML method predicted pattern and topology for 4-element failures with the measured data.

5.2.3. Comparison Plots for 4-Element Failures

In Fig. (5.19) given below, it can be seen that the ML performs consistently better or sometimes the same as the GA method. Due to the additional non-linearities present in the measured data, the GA method in most cases fails to detect higher than 2 elements correctly out of 4. But in full-wave simulated data both the methods, perform better and the ML method consistently predicts almost all the elements correctly with some exceptions. With a higher sample set the need and superiority of the ML method can be further established.

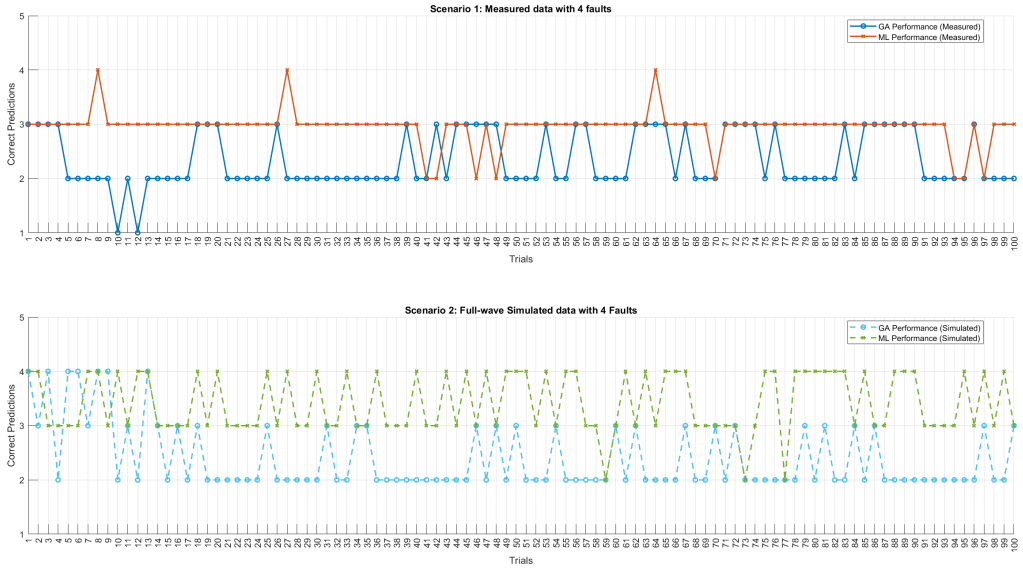

Figure 5.19: Comparison plot for the 4-element failures using simulated and measured data.

5.3. 2-Element Failures

5.3.1. GA Results

The particular topology result discussed here is when both GA and ML predicted one element correctly. In this case, the different patterns and sensor dB values are to be compared to understand the behaviour of each method.

Full-wave Simulated Data

The parameters used for this simulation are given in Table (5.4).

Table 5.4: Optimization Parameters - Full-wave simulated data

Parameters	Values
Number of faults	2
Number of realizations	25
Number of Iterations	1000
Crossover probability	0.4
Mutation Probability	0.03
Population Size	50

An example faulty pattern with 2 failures is shown in Fig.(5.20).

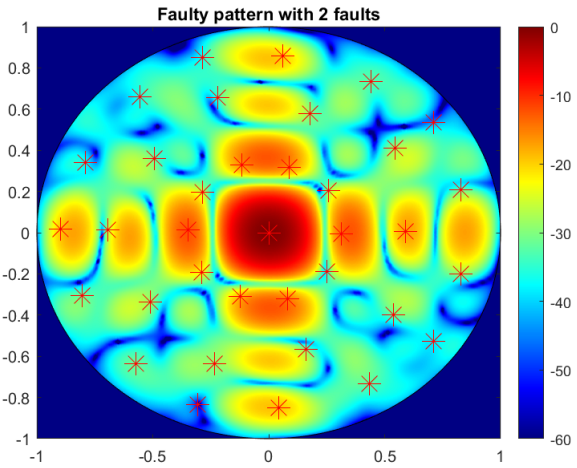

Figure 5.20: UV plot of full-wave simulated pattern for 2-element failure case where red stars indicating the DOME sampling points.

The results obtained from the GA method are shown in Fig.(5.21). The pattern obtained from the GA has some distinct changes in the sidelobe region, especially near the Outer-Middle ring nodes. The main beam and the shape of the pattern are mostly preserved but there is a single element error. Moreover, the incorrect element detected by the GA does not indicate the correct region of the target faulty element as well.

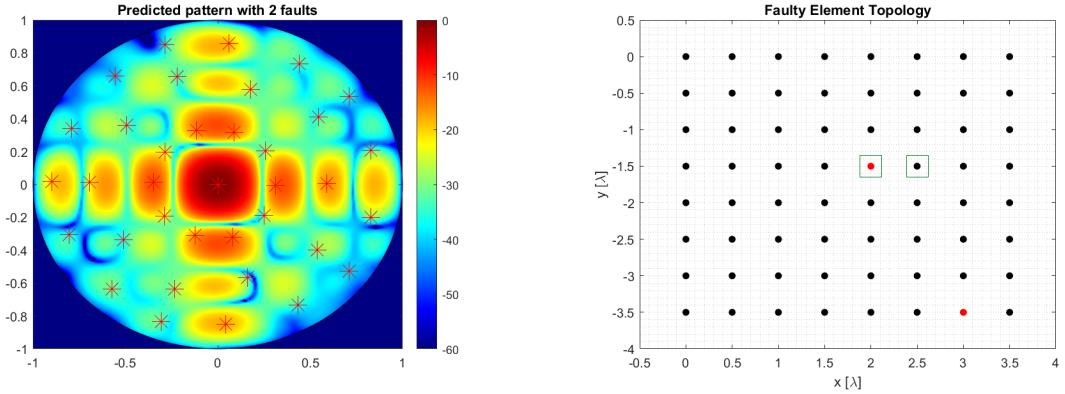

(a) Full-wave simulated pattern with 2-element failures where red stars indicating the DOME sampling points

(b) Array element topology with predictions where red dots indicate the faulty elements, green boxes indicate the predictions

Figure 5.21: GA method predicted pattern and the topology for 2-element failure case.

Measured Data

The results for the same topology considered in Section (5.3.1) are compared in the measured data scenario as well. Here, the GA method fails to predict any faulty elements but to compare the differences in the pattern and the cause for such failure can be discussed. The parameters used for this simulation are given in Table (5.5).

Table 5.5: Optimization Parameters - Measured data

Parameters	Values
Number of faults	2
Number of realizations	25
Number of Iterations	1000
Crossover probability	0.35
Mutation Probability	0.03
Population Size	50

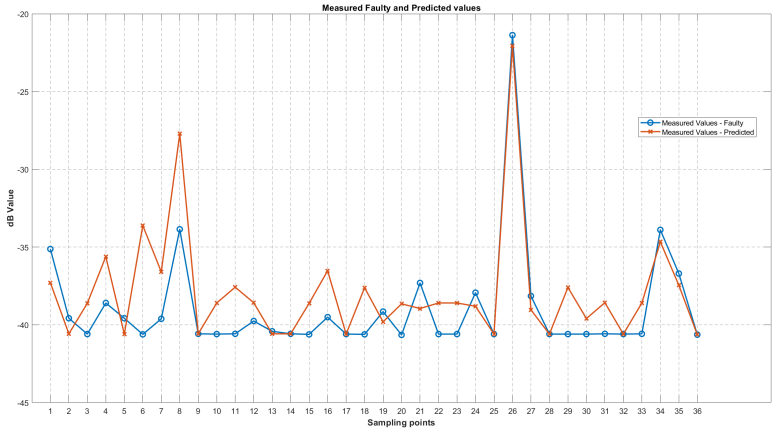

(a) Measured and GA predicted results comparison for the 2-element failure case

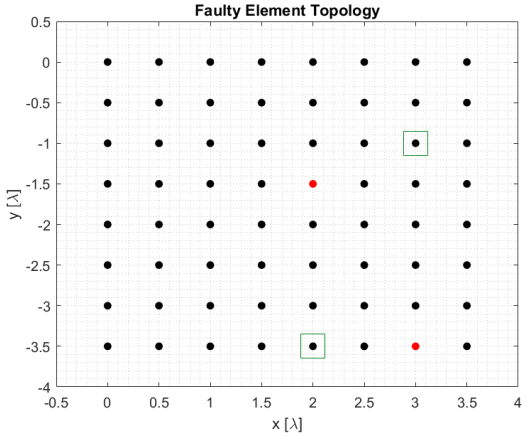

(b) Array element topology with original faults and predictions where red dots indicate the faulty elements, green boxes indicate the predictions

Figure 5.22: GA method predicted pattern and topology for 2-element failure case with measured data.

The predicted pattern varies from the original pattern, the region of the fault is not accurately diagnosed as well. A reason other than the complexity of the data could also be the number of realizations. Hence, at the expense of computational power, if the optimizer is run for a higher number of iterations then the results will most likely improve. But for using similar parameters for both GA and ML, the solutions provided by ML are more desirable, this will be discussed in the following section (5.3.2).

5.3.2. ML Results

The results using the purely data-driven model are discussed for measured data. For a fair comparison, the same topology is chosen and is compared with the full-wave simulated result as well. The modified model from the original fully connected model are applied for the varying faults case as well (see Section (4.6) for details).

Full-wave Simulated Data

The original topology and pattern are described in Section (5.3.1) using Fig. (5.20). Now, the results from the ML method is discussed for the scenario given in Fig. (5.23).

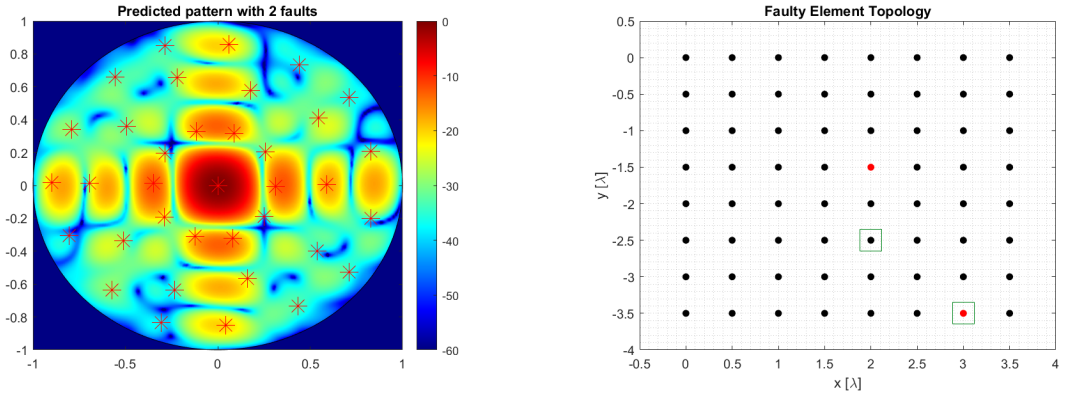

(a) Measured pattern comparison with 2 faults where red stars indicating the DOME sampling points

(b) Array element topology where red dots indicate the faulty elements, green boxes indicate the predictions

Figure 5.23: ML results - Predicted pattern and topology for 2 failures (Full-wave simulated data)

There are some noticeable changes in the far sidelobes but the overall normalized power and pattern are maintained. Furthermore, the incorrect prediction is near the region of the actual target element. This also proves the ability of the ML method to achieve regional diagnosis when very less faults are considered.

Measured Data

In this subdivision, the results from the measurement data are analysed and compared with the original faulty pattern values. The same topology is considered to maintain uniformity in the results and have a fair comparison.

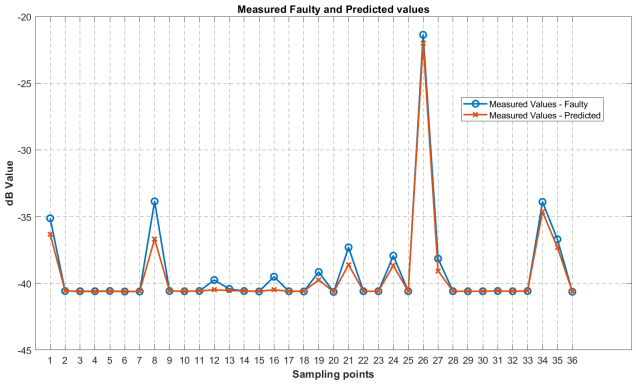

Figure 5.24: Faulty and ML predicted values for 2 failures using measured data

5.3.3. Comparison Plots for 2-Element Failures

The Fig.(5.25) given below, represents the results from 100 trials of the GA and ML methods for 2 failure cases. In the measured data case, the GA performs poorly in comparison to the ML method. ML predicts mostly 50% of the elements correctly which is considerably good for just 2 element failures in a practical system. As expected in the full-wave simulated case both the methods perform relatively better compared to the measured. The number of completely correct predictions is also improved.

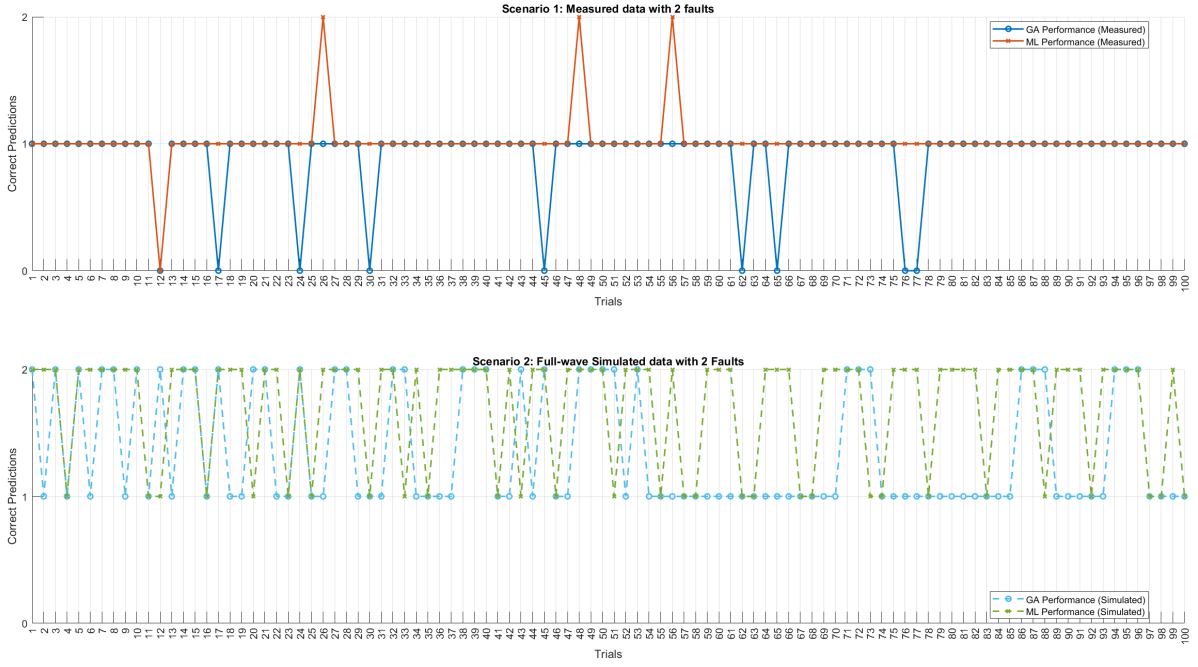

Figure 5.25: Comparison plot for 2-element failures using simulated and measured data.

5.4. Ring Analysis

In this section, the discussion is focused on the number of sampling points used for carrying out the fault diagnosis of the antenna-under-test (AUT). As the structure of the dome is not fully uniform. So the set of sampling points can be segregated into 'rings'. Physically these rings do not exist, they are used to explain the sensor nodes better and conduct the analysis in a structured way. The two scenarios that are explored are as follows,

- Outer Ring (15 sampling points);
- Outer-Middle Ring (25 sampling points).

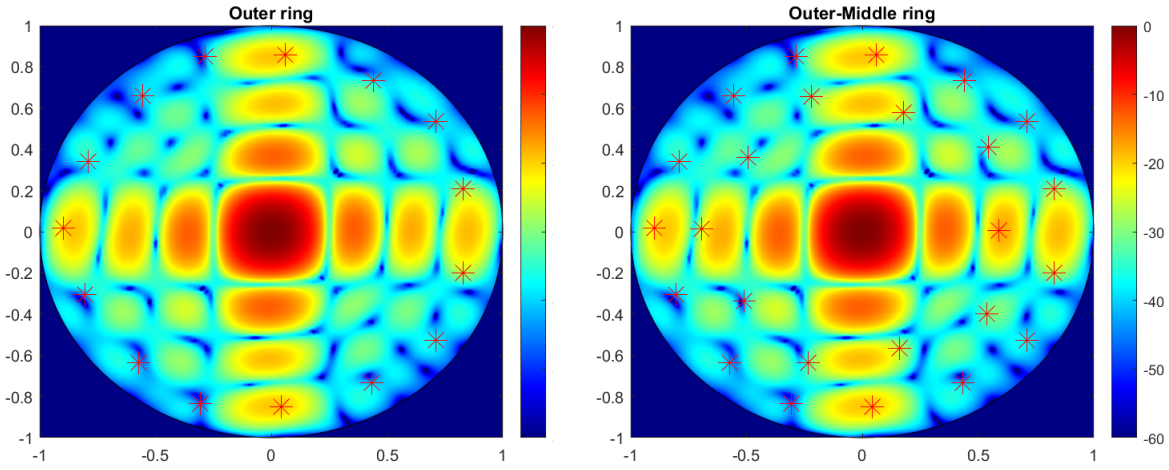

(a) Outer ring sampling points **(b)** Outer-Middle ring sampling points

Figure 5.26: Ring Analysis scenarios where red stars indicating the DOME sampling points.

The choice for this particular combination of rings was to ensure that the main beam radiation was not blocked (especially by the inner sensor nodes). Furthermore, study the importance of using the far sidelobe information and working with a specific combination of sampling points.
The results from studying the various rings can be further divided based on the number of faults. This is carried out to understand the effect of rings and the number of faults on the performance of the respective approaches.

5.4.1. 2-Element Fault Scenarios

Table 5.6: Success Ratios for Different Rings

Rings	Minimum Success Ratio	Average Success Ratio	Maximum Success Ratio
Outer Ring	0%	42%	50%
Outer-Middle Ring	50%	51%	100%

To visualize some of the results, the Fig. (5.27) is plotted for 100 trials. The performance of Outer - Middle ring as expected is higher than the Outer ring (lesser number of sampling points).

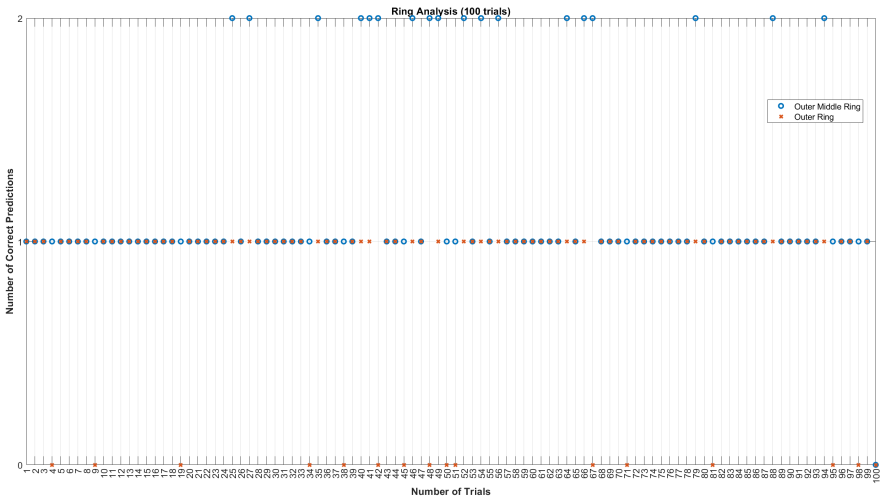

Figure 5.27: Comparison plot with Outer ring and Outer-Middle ring with 2 failures (Measured data).

5.4.2. 4-Element Fault Scenarios

Table 5.7: Success Ratios for Outer and Outer-Middle Rings

Rings	Minimum Success Ratio	Average Success Ratio	Maximum Success Ratio
Outer Ring	50%	57.5%	75%
Outer-Middle Ring	50%	70%	100%

Similar to the results displayed in the previous section, the Fig. (5.28) is plotted for 100 trials. The trend where the Outer-Middle ring performs better than the Outer ring remains the same. As the number of faults increases, there are more changes in the pattern so it is possible to track more than the 2 faulty cases. This can be seen in the next section as well.

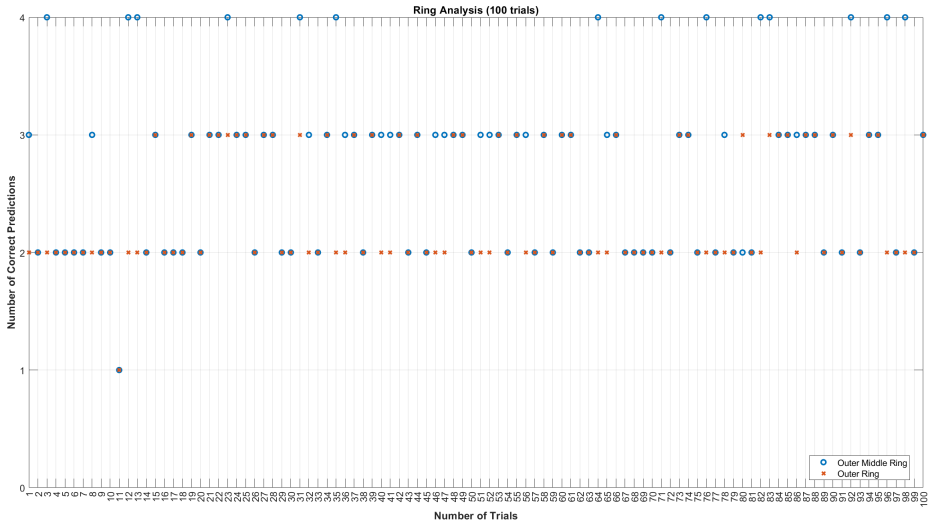

Figure 5.28: Comparison plot with Outer ring and Outer-Middle ring with 4 failures (Measured data).

5.4.3. 8-Element Fault Scenarios

Table 5.8: Success Ratios for Outer and Outer-Middle Rings in the Experiment

Rings	Minimum Success Ratio	Average Success Ratio	Maximum Success Ratio
Outer Ring	50%	61%	75%
Outer-Middle Ring	75%	81%	100%

The first 100 trials in the validation set are plotted here, in Fig. (5.29) for a fair comparison.

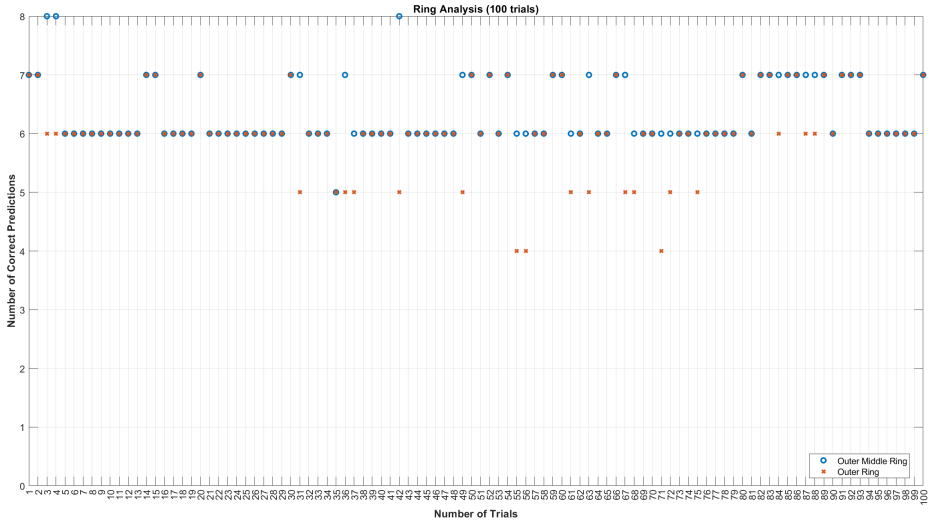

Figure 5.29: Comparison plot with Outer ring and Outer-Middle ring with 8 failures (Measured data).

5.5. Conclusions

This chapter discusses the different results obtained from both optimizers. The main parts are, 2,4,8 - Element failures, Ring analysis for the different types of data like Array factor, full-wave simulated and measured data. Through the fault analysis, it can be inferred that with a higher number of faults a higher accuracy can be achieved, as the changes in the pattern are also more distinct in comparison lesser number of faults. Furthermore, the amount of data used also proves to be important in the fault detection process. For all three types of data, ML outperforms the GA method with respect to computational time and successful predictions. An analysis is conducted for the performance with lesser number of sampling points as well. The Outer-Middle ring (25 sampling points) performs better than the Outer ring (15 sampling points) for varying fault scenarios. A more detailed description of the conclusions will be provided in the Conclusions chapter (6).

6

Conclusion and Recommendations

The main conclusions and contributions to existing literature along with future recommendations are mentioned in this chapter.

6.1. Conclusions

This thesis proposes a novel machine learning framework for fast detection of faulty elements in active phased arrays (mm-wave frequencies) under non-linearity effects caused by mutual coupling and IC behaviour. A comparative analysis between a bench-marked genetic algorithm and the proposed machine learning method is conducted for the simulated and measured pattern data of an 8x8 array. Deterministic and statistical studies are carried out to understand the theory behind the behaviour of these faults and how complex the problem is when random fails are considered. It is demonstrated that the machine learning algorithm is faster, requires fewer close-form solutions to arrive at the optimum result, and models the full-wave simulated and measured data better leading to a superior detection performance. This generic result is further validated and quantified by varying the number of failed elements and by reducing the number of sampling points to enable in-field operation with continuous pattern monitoring.
Using the performance metric success ratio defined in equation (4.8) in section (4.6.1). Table (6.1) is formed, which summarises the key outputs of the thesis.

- **Full ring:** 3 rings + center point;
- **Outer-Middle ring:** 25 sampling points;
- **Outer ring:** 15 sampling points.

Table 6.1: Comprehensive results for GA and ML methods with varying parameters.

Method	Data Type	No. of Sampling points	Number of faults	Minimum Success ratio (%)	Average Success ratio (%)
ML	Array factor	36	8	75%	96.875%
GA	Array factor	36	8	75%	94.625%
ML	Full-wave simulated	36	8	75%	93%
GA	Full-wave simulated	36	8	50%	61%
ML	Measured	36	8	62.5%	81.5%
GA	Measured	36	8	25%	47.375%
ML	Measured	25	8	75%	81%
GA	Measured	25	8	25%	45%
ML	Measured	15	8	50%	61%
GA	Measured	15	8	25%	41%
ML	Full-wave simulated	36	4	50%	85%
GA	Full-wave simulated	36	4	50%	60%
ML	Measured	36	4	50%	73.75%
GA	Measured	36	4	25%	58%
ML	Measured	25	4	50%	70%
ML	Measured	15	4	50%	57.5%
ML	Full-wave simulated	36	2	50%	82%
GA	Full-wave simulated	36	2	50%	68%
ML	Measured	36	2	0%	52%
GA	Measured	36	2	0%	45.5%
ML	Measured	25	2	50%	51%
ML	Measured	15	2	0%	42%

The ML provides improved performance compared to the GA method in all the cases discussed in Table (6.1). The average success ratio in the case of the measurement data has an improvement from around 50% to 80% while comparing the GA against the ML.

An important conclusion from varying the number of faults is to establish that the methods are applicable to a practical number of failures in an operational system. In this thesis, the main starting point was the 8 faults scenario (12.5%) and multiple studies were carried out. According to literature, the practical systems have around 10% or lesser failure rates. Whereas for simulated or array factor data very high percentages are considered, sometimes even higher than 50%. Hence, a comprehensive study involving varying number of faults was essential to further study the applications of this thesis. It can be seen from the tabulation (Table. (6.1) that even with lesser number of faults, the performance is not reduced drastically. The ML as expected performs better than the GA for the measured data. In the simulated and array factor cases, GA performs better than the higher fault scenarios as there is a smaller search space and can converge more easily compared to the 8 fault scenario.

The results from the fault analysis and the ring analysis also imply the same. The outer-middle ring has 25 sampling points out of the total 36 so it is still able to retain the majority of the information hence, has a lower but similar performance to using all the dome sampling points. Whereas the outer ring indicates poorer performance than expected compared to the outer-middle ring. For varying numbers of faults, the performance drops for both algorithms as there are comparatively fewer changes in the pattern when a larger number of faults is considered. Mostly, the ML performs quite well compared to the GA and also detects 50% of the elements for the two faults scenario.

6.2. Recommendations

The following areas can be considered as recommendations for extending the work conducted in this thesis,

- Optimization of hyper-parameters and selection of best machine learning model with differing input types.
- Including steered beams or multi-frequency operation in the dataset to improve detection performance and analyzing the trade-offs.
- Studying the impact of increasing the number of spatial sampling points by adding movable components in the antenna dome (e.g. shifting the AUT in xy plane or rotating the dome 'rings').
- Extension from fail detection to fast pattern compensation using ML.
- Extension from failure detection to more complex amplitude-phase variation characterization for calibration.

Bibliography

[1] Xiaoxiong Gu, Duixian Liu, and Bodhisatwa Sadhu. “Packaging and Antenna Integration for Silicon-Based Millimeter-Wave Phased Arrays: 5G and Beyond”. In: *IEEE Journal of Microwaves* 1.1 (2021), pp. 123–134. DOI: 10.1109/JMW.2020.3032891.

[2] “IEEE Recommended Practice for Antenna Measurements”. In: *IEEE Std 149-2021 (Revision of IEEE Std 149-1977)* (Feb. 2022), pp. 1–207. DOI: 10.1109/IEEESTD.2022.9714428.

[3] Alan J. Fenn et al. *The Development of Phased-Array Radar Technology*. Lincoln Laboratory Journal, 2000.

[4] C.A. Balanis. *Antenna Theory: Analysis and Design*. Wiley, 2012. ISBN: 9781118585733. URL: https://books.google.nl/books?id=v1PSZ48DnuEC.

[5] Choudhury Balamati and RM Jha. “Soft Computing in Electromagnetics: Methods and Applications”. In: 2016. URL: https://api.semanticscholar.org/CorpusID:264247326.

[6] Robert Mailloux. Artech, 2017. ISBN: 9781630815080. URL: https://ieeexplore.ieee.org/document/9100156.

[7] Solon J. Spiegel. “Analysis of Impairments, Error Correction and Evaluation of Adaptive Antenna Arrays Based on Vector Modulators Beamforming ICs”. In: *2022 IEEE Microwaves, Antennas, and Propagation Conference (MAPCON)*. Dec. 2022, pp. 1255–1260. DOI: 10.1109/MAPCON56011.2022.10047173.

[8] T.J. Peters. “A conjugate gradient-based algorithm to minimize the sidelobe level of planar arrays with element failures”. In: *IEEE Transactions on Antennas and Propagation* 39.10 (Oct. 1991), pp. 1497–1504. ISSN: 1558-2221. DOI: 10.1109/8.97381.

[9] Fawad Zaman et al. “Backtracking Search Optimization Paradigm for Pattern Correction of Faulty Antenna Array in Wireless Mobile Communications”. In: *Wireless Communications and Mobile Computing* 2019 (July 2019), pp. 1–17. DOI: 10.1155/2019/9046409.

[10] L.A. Wegrowicz and R. Pokuls. “Inverse problem approach to array diagnostics”. In: *Antennas and Propagation Society Symposium 1991 Digest*. 1991, 1292–1295 vol.2. DOI: 10.1109/APS.1991.175085.

[11] R. A. Coesoij et al. “Calibration approaches in Multi-Node Antenna Characterization Setups”. In: *2023 100th ARFTG Microwave Measurement Conference (ARFTG)*. 2023, pp. 1–4. DOI: 10.1109/ARFTG56062.2023.10148881.

[12] NXP. *Designing a 5G mmWave antenna means balancing tradeoffs*. https://www.nxp.com/company/blog/designing-a-5g-mmwave-antenna-means-balancing-tradeoffs:BL-DESIGNING-A-5G-MMWAVE. Accessed: 2024-06-26.

[13] Yanki Aslan et al. “Thermal-aware synthesis of 5g base station antenna arrays: An overview and a sparsity-based approach”. In: *IEEE Access* 6 (2018). ISSN: 21693536. DOI: 10.1109/ACCESS.2018.2873977.

[14] F. A. Musters et al. “The Antenna Dome Real-Time Distributed Antenna Pattern Characterization System”. In: Institute of Electrical and Electronics Engineers Inc., 2021. ISBN: 9780738112480. DOI: 10.1109/ARFTG52261.2021.9640079.

[15] M. Steyskal and R.J. Mailloux. “Generalization of a phased array error correction method”. In: *IEEE Antennas and Propagation Society International Symposium. 1996 Digest*. Vol. 1. July 1996, 506–509 vol.1. DOI: 10.1109/APS.1996.549648.

[16] Tutorials Point. *Antenna Theory - Near and Far Fields*. https://www.tutorialspoint.com/antenna_theory/antenna_theory_near_and_far_fields.htm. Accessed: 2024-07-22.

[17] M. Ayyaz Qureshi, Carsten H. Schmidt, and Thomas F. Eibert. “An Effective Nonredundant Sampling Representation for Planar Near-Field Antenna Measurements”. In: *Lehrstuhl für Hochfrequenztechnik, Technische Universität München* (2021).

[18] J.J. Lee et al. “Near-field probe used as a diagnostic tool to locate defective elements in an array antenna”. In: *IEEE Transactions on Antennas and Propagation* 36.6 (1988), pp. 884–889. DOI: 10.1109/8.1192.

[19] Yanki Aslan et al. “Heuristic Over-the-Air Calibration of Beamformer ICs in Active mm-Wave Phased Arrays”. In: *2023 IEEE Conference on Antenna Measurements and Applications (CAMA)*. 2023, pp. 840–845. DOI: 10.1109/CAMA57522.2023.10352655.

[20] Raffaele Moretta et al. “Array Faulty Element Diagnostics by Few Phaseless Data and Convex Optimization”. In: *2023 17th European Conference on Antennas and Propagation (EuCAP)*. Mar. 2023, pp. 1–4. DOI: 10.23919/EuCAP57121.2023.10133588.

[21] Huapeng Zhao et al. “Near-field-based array failure diagnosis using sparse source reconstruction”. In: *2017 Asia-Pacific International Symposium on Electromagnetic Compatibility (APEMC)*. June 2017, pp. 309–311. DOI: 10.1109/APEMC.2017.7975490.

[22] Oluwole John Famoriji et al. “Active Antenna Array Diagnosis from Far-Field Measurements”. In: *2018 IEEE International Conference on Integrated Circuits, Technologies and Applications (ICTA)*. 2018, pp. 38–39. DOI: 10.1109/CICTA.2018.8706071.

[23] F.A. Musters. “Real-Time 3D Characterization of Antenna Systems”. Supervised by E.W. McCune, M. Spirito, and M.A.P. Pertijs. Master’s thesis. Delft University of Technology: Electrical Engineering, Mathematics and Computer Science, 2019. URL: http://resolver.tudelft.nl/uuid:bd3966f1-70d2-4f55-be5b-8c4e8d767a65.

[24] Benjamin Fuchs, Laurent Le Coq, and Marco Donald Migliore. “Fast Antenna Array Diagnosis from a Small Number of Far-Field Measurements”. In: *IEEE Transactions on Antennas and Propagation* 64.6 (June 2016), pp. 2227–2235. ISSN: 1558-2221. DOI: 10.1109/TAP.2016.2547023.

[25] M. Levitas, D.A. Horton, and T.C. Cheston. “Practical failure compensation in active phased arrays”. In: *IEEE Transactions on Antennas and Propagation* 47.3 (Mar. 1999), pp. 524–535. ISSN: 1558-2221. DOI: 10.1109/8.768788.

[26] Guo Bai et al. “Rapid Failure Diagnosis of Impaired Linear Antenna Arrays Based on Matrix Pencil Method”. In: *IEEE Antennas and Wireless Propagation Letters* 21.8 (2022), pp. 1708–1712. DOI: 10.1109/LAWP.2022.3178435.

[27] O.M. Bucci et al. “Accurate diagnosis of conformal arrays from near-field data using the matrix method”. In: *IEEE Transactions on Antennas and Propagation* 53.3 (2005), pp. 1114–1120. DOI: 10.1109/TAP.2004.842656.

[28] Navaamsini Boopalan, Agileswari K. Ramasamy, and Farrukh Nagi. “A Comparison of Faulty Antenna Detection Methodologies in Planar Array”. In: *Applied Sciences (Switzerland)* 13 (6 Mar. 2023). ISSN: 20763417. DOI: 10.3390/app13063695.

[29] Jing Miao et al. “An improved method of diagnosis of failed elements in arrays based on far-field radiation pattern”. In: *2016 Progress in Electromagnetic Research Symposium (PIERS)*. 2016, pp. 467–471. DOI: 10.1109/PIERS.2016.7734367.

[30] Amalendu Patnaik et al. “An ANN Application for Fault Finding in Antenna Arrays”. In: *IEEE Transactions on Antennas and Propagation* 55.3 (Mar. 2007), pp. 775–777. ISSN: 1558-2221. DOI: 10.1109/TAP.2007.891557.

[31] Atul M. Kulkarni, Shyam S. Pattnaik, and Garima Saini. “Genetic-CNN based fault diagnosis in antenna array”. In: 2023. DOI: 10.1109/ISAP57493.2023.10389126.

[32] He Ming Yao et al. “Antenna Array Diagnosis Using a Deep Learning Approach”. In: *IEEE Transactions on Antennas and Propagation* 72.6 (2024), pp. 5396–5401. DOI: 10.1109/TAP.2024.3387689.

[33] O.M. Bucci, A. Capozzoli, and G. D’Elia. “Diagnosis of array faults from far-field amplitude-only data”. In: *IEEE Transactions on Antennas and Propagation* 48.5 (May 2000), pp. 647–652. ISSN: 1558-2221. DOI: 10.1109/8.855482.

[34] Yanki Aslan et al. “Trade-offs between the quality of service, computational cost and cooling complexity in interference-dominated multi-user SDMA systems”. In: *IET Communications* 14.1 (2020), pp. 144–151. DOI: https://doi.org/10.1049/iet-com.2019.0206. eprint: https://ietresearch.onlinelibrary.wiley.com/doi/pdf/10.1049/iet-com.2019.0206. URL: https://ietresearch.onlinelibrary.wiley.com/doi/abs/10.1049/iet-com.2019.0206.

[35] Ryan J. Chaky et al. “Analysis and Recovery Optimization of Sporadic Reflectarray Phase Failures Based on Array Factors”. In: vol. 2022-October. 2022. DOI: 10.1109/PAST49659.2022.9974978.

[36] S. Kirkpatrick, C. D. Gelatt, and M. P. Vecchi. “Optimization by Simulated Annealing”. In: *Science* 220.4598 (1983), pp. 671–680. DOI: 10.1126/science.220.4598.671. eprint: https://www.science.org/doi/pdf/10.1126/science.220.4598.671. URL: https://www.science.org/doi/abs/10.1126/science.220.4598.671.

[37] Wenlong Liu et al. “A low complexity detection for the binary MIMO system using Lagrange multipliers”. In: *2013 International Joint Conference on Awareness Science and Technology Ubi-Media Computing (iCAST 2013 UMEDIA 2013)*. 2013, pp. 486–491. DOI: 10.1109/ICAwST.2013.6765489.

[38] Antonio LaTorre et al. “A prescription of methodological guidelines for comparing bio-inspired optimization algorithms”. In: *Swarm and Evolutionary Computation* 67 (2021). ISSN: 22106502. DOI: 10.1016/j.swevo.2021.100973.

[39] Pramod Kumar, Ashutosh Kedar, and N. K. Vishwakarma. “Genetic Algorithm Aided Synthesis of Low SLL Antenna Array Utilizing Position Optimization based on Zoning Technique”. In: *2018 IEEE Indian Conference on Antennas and Propogation (InCAP)*. 2018, pp. 1–4. DOI: 10.1109/INCAP.2018.8770850.

[40] Xiaopeng Fang. “Engineering design using genetic algorithms”. In: 2007. URL: https://api.semanticscholar.org/CorpusID:108038756.

[41] Bryan Raj et al. “A Hybrid Sperm Swarm Optimization and Genetic Algorithm for Unimodal and Multimodal Optimization Problems”. In: *IEEE Access* 10 (2022), pp. 109580–109596. ISSN: 2169-3536. DOI: 10.1109/ACCESS.2022.3208169.

[42] Jiang Wu et al. “Data Pipeline Training: Integrating AutoML to Optimize the Data Flow of Machine Learning Models”. In: *2024 7th International Conference on Advanced Algorithms and Control Engineering (ICAACE)*. Mar. 2024, pp. 730–734. DOI: 10.1109/ICAACE61206.2024.10549260.

[43] Lateef Adesola Akinyemi et al. “Enhancing Chronic Kidney Disease Prediction Through Data Preprocessing Optimization and Machine Learning Techniques”. In: *2023 International Conference on Electrical, Computer and Energy Technologies (ICECET)*. 2023, pp. 1–6. DOI: 10.1109/ICECET58911.2023.10389513.

[44] Ian J Goodfellow, Jonathon Shlens, and Christian Szegedy. “Explaining and Harnessing Adversarial Examples”. In: *arXiv preprint arXiv:1412.6980* (2015). DOI: 10.48550/arXiv.1412.6980. URL: https://arxiv.org/abs/1412.6980.

[45] Noor Azwana Mat Ariff and Amelia Ritahani Ismail. “Study of Adam and Adamax Optimizers on AlexNet Architecture for Voice Biometric Authentication System”. In: *2023 17th International Conference on Ubiquitous Information Management and Communication (IMCOM)*. 2023, pp. 1–4. DOI: 10.1109/IMCOM56909.2023.10035592.

[46] Zhiping Li, Peng Huo, and Jianhua Wu. “Fast Antenna Array Diagnosis Based on Shifted Base Mode Character From Sparse Measurements”. In: *IEEE Transactions on Antennas and Propagation* 70.12 (2022), pp. 12163–12176. DOI: 10.1109/TAP.2022.3209212.

[47] Towards Data Science. “Useful plots to diagnose your neural network”. In: *Medium* (Jan. 2019). URL: https://towardsdatascience.com/useful-plots-to-diagnose-your-neural-network-521907fa2f45.